PHYSICAL REVIEW B VOLUME 49, NUMBER 22 1 JUNE 1994-II

Flux-trapping phenomena in sintered tubes of high-T_c superconductors

Selahattin Çelebi
Physics Department, Karadeniz Technical University, Trabzon, Turkey 61080

M. A. R. LeBlanc
Physics Department, University of Ottawa, Ottawa, Canada K1N 6N5

(Received 20 December 1993; revised manuscript received 24 February 1994)

The remanent magnetic flux density trapped in the cavity and in the wall of sintered tubes of Y-Ba-Cu-O and Bi-Sr-Ca-Cu-O was measured as a function of H_{cool}, the axial magnetic field present during field cooling and then removed, and of H_{cycle}, the axial magnetic field impressed and removed after zero-field cooling. For both procedures the two specimens exhibit very different behavior. A simple critical-state model which takes into account the return field of the magnetized grains quantitatively reproduces all of our observations and the corresponding data reported by others.

I. INTRODUCTION

Since magnetic flux permanently trapped in the cavity of hollow cylinders of type-II superconductors can provide a useful environment for experiments in steady magnetic fields, this property has attracted great interest.[1-28] In some circumstances this setup offers a simple substitute for a wire-wound superconducting solenoid and may be much easier to fabricate. Also, an axially magnetized superconducting tube can serve as a permanent magnet almost as effective but lighter than one using a solid rod of the same material and outer dimensions.[7,10,17,21,24]

$\langle B_z \rangle_{\text{hole}}$, the remanent magnetic flux density trapped in the cavity of hollow cylinders of sintered high-T_c superconductors, exhibits a variety of behavior as a function of the magnitude of $H_{\parallel}$, the axial magnetic field which has been applied to magnetize the tube. Two different modes of behavior have been reported. (a) In some cases, the steep rise of $\langle B_z \rangle_{\text{hole}}$ versus $H_{\parallel}$ traces a "knee" or "kink" which is followed by a broad region of slow monotonic growth and then a plateau.[1,2] (b) In other cases, $\langle B_z \rangle_{\text{hole}}$ vs $H_{\parallel}$ forms a peak also followed by a plateau.[3,19] In some instances, the descent of $\langle B_z \rangle_{\text{hole}}$ from the summit of the peak can traverse zero and lead to a reversal of the sign of the trapped flux.[3,5]

Several workers have indicated that the magnetic flux of the magnetized grains "returning" (i) through the cavity and (ii) through the "matrix" joining the grains can account for the different behaviors just described.[1-5,19] The latter is thought to have a strong effect on I_c, the critical intergranular current induced to circulate azimuthally around the tube by the removal of $H_{\parallel}$, and hence on the magnetic field trapped in the cavity.

An important feature in our investigation is that we monitor not only $\langle B_z \rangle_{\text{hole}}$ vs $H_{\parallel}$ but also $\langle B_z \rangle_{\text{wall}}$, the spatial average of the magnetic flux density in the wall of the tube, vs $H_{\parallel}$. The combination of these two sets of data enables us to assess the magnitude of the magnetization of the grains and its effect on I_c.

Further, we exploit two standard procedures for trapping magnetic flux in the tubes. These are denoted H_{cool} and H_{cycle} procedures. The complementary data obtained by using these two different procedures enable us to evaluate the dependence of j_{cm} and j_{cg}, the intergrain and intragrain critical current densities on the magnetic field in the low-field range.

We report on measurements on tubes of two different high-T_c materials which display the two different types of behavior described above under (a) and (b). We apply the ideas just mentioned to the analysis of our observations in a simple framework which not only quantitatively accounts for our results but also reproduces data already reported in the literature.[1-5,19]

II. EXPERIMENTAL ARRANGEMENT AND PROCEDURES

$\langle B_z \rangle_{\text{hole}}$ and $\langle B_z \rangle_{\text{wall}}$ are continuously monitored using two pickup coil systems which separately feed amplifier integrators which drive the Y axis of XY recorders. The X axes are driven by a signal proportional to $H_{\parallel}$ provided by the voltage across a shunt in the circuit of the solenoid generating $H_{\parallel}$.

The inner pickup coil monitoring $\langle B_z \rangle_{\text{hole}}$, the spatial average of the axial flux density threading the cavity, extends along the central half of the length of a tube specimen. The determination of $\langle B_z \rangle_{\text{wall}}$, the axial magnetic flux density permeating the wall of the tube, is a composite measurement obtained as follows. A pickup coil intimately embracing the waist of the tube specimen records $\Delta\Phi_{z,\text{total}}$, the change in the total axial magnetic flux threading this pickup coil. Since, by definition,

$$\begin{aligned}\Phi_{z,\text{total}} &= \langle B_z \rangle_{\text{total}} \pi R_o^2 \\ &= \Phi_{z,\text{hole}} + \Phi_{z,\text{wall}} \\ &= \langle B_z \rangle_{\text{hole}} \pi R_i^2 + \langle B_z \rangle_{\text{wall}} \pi (R_o^2 - R_i^2) \qquad (1)\end{aligned}$$

(where R_i and R_o are the inner and outer radius of the tube), we can determine $\langle B_z \rangle_{\text{wall}}$ by subtracting the signal generated by the inner pickup coil, which detects $\Delta\Phi_{z,\text{hole}}$, from that of the outer pickup coil, either electronically or digitally.

The signal from the inner pickup coil monitoring $\langle B_z \rangle_{\text{hole}}$ is calibrated by applying $H_\parallel$ with the tube maintained in the normal state. The signal from the outer pickup coil is calibrated in two steps. First we determine the low range of $H_\parallel$ over which the magnetization of the tube is linear. In this weak-field range, no magnetic flux is entering across the outer surface of the tube except into the relatively minute penetration-depth region. Now $H_\parallel$ is applied to the virgin (zero-field-cooled) tube to a value well below the limit of this linear range and then maintained fixed. Then the sample tube is driven into the normal state by means of an electric heater. The signal S_o detected at this juncture by the outer pickup coil/integrator/amplifier corresponds to the entry of axial magnetic flux $\Delta\Phi_{z,\text{total}}$ into the wall and cavity, hence,

$$S_o \propto \Phi_{z,\text{total}} = \mu_0 H_\parallel \pi R_o^2 \ . \qquad (2)$$

The electric heater consists of a single layer coil of 38 B&S Manganin wire bifilarly (noninductively) wound and uniformly and directly embracing the entire external surface of the tube specimen. A thermal barrier of a few layers of masking tape wrapped around the specimen (outside the outer pickup coil) minimizes the heat input needed to attain temperatures above T_c.

The axial magnetic field $H_\parallel$ provided by a copper wire solenoid 18 cm long with inner and outer diameters of 4.0 and 5.5 cm for the winding (generating 37.7 mT/A) is uniform within a few percent over the volume of the specimens. The solenoid and the specimen bathe in liquid nitrogen at atmospheric pressure.

Two standard procedures, denoted H_{cool} and H_{cycle} procedures, were exploited to trap a remanent flux in the tubes. In the H_{cool} procedure, the tube is allowed to cool from above T_c to the ambient 77-K temperature in static axial field $H_\parallel$, denoted H_{cool} (i.e., the tube is field cooled). Then $H_\parallel = H_{\text{cool}}$ is slowly reduced to zero. In the H_{cycle} procedure, the tube is first zero-field cooled from above T_c to 77 K. Then $H_\parallel$ is slowly raised to a selected value denoted H_{cycle}, which is then gradually removed. In both procedures, the magnetic flux density trapped in the cavity and in the wall, denoted $\langle B_z \rangle_{\text{hole}}$ and $\langle B_z \rangle_{\text{wall}}$, are measured simultaneously by recording the signal from the inner and outer pickup coils/integrator/amplifier systems when the tube is driven into the normal resistive state by raising its temperature through T_c by means of the electric heater. This causes the inter- and intragranular persistent currents which sustain the remanent magnetic flux to decay quickly and thereby release this trapped flux.

TABLE I. Dimensions of tubes.

Sample	Inner diameter (cm)	Outer diameter (cm)	Length (cm)
BiSCCO	1.40	1.72	3.70
YBCO	1.50	3.00	5.00

We report on flux-trapping behavior at 77 K in hollow cylinders of two different high-T_c superconductors, namely, 2223 phase $(\text{Bi}_{0.9}\text{Pb}_{0.1})_2\text{Sr}_2\text{Ca}_2\text{Cu}_3\text{O}_{10}$ and $\text{YBa}_2\text{Cu}_3\text{O}_{7-x}$, where $x \approx 0.15$. These will be denoted BiSCCO and YBCO for brevity throughout this paper. Table I lists the dimensions of the two tubes in cm.

III. RESULTS AND DISCUSSION

A. General comments

Figures 1–4 display our data on flux trapping by the H_{cool} and H_{cycle} procedures for the YBCO and BiSCCO tubes. A quick inspection of these figures reveals that the two tubes exhibit two different modes of flux-trapping behavior in the cavity. For the BiSCCO tube, $\langle B_z \rangle_{\text{hole}}$ rises monotonically to a plateau whereas in the YBCO tube $\langle B_z \rangle_{\text{hole}}$ describes a peak followed by a decline to a low-lying plateau. Examples of these two regimes have already been reported by other workers.[1–3,5,19] We propose a simple model that generates a "spectrum" of behavior which includes our results and encompasses the behavior previously reported.[1–3,5,19] This phenomenological model is based on concepts put forward and exam-

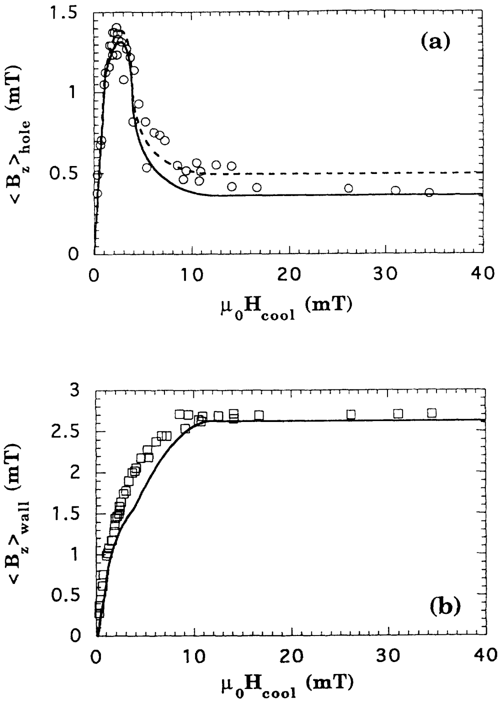

FIG. 1. YBCO tube at 77 K. (a) Data points are experimental and display $\langle B_z \rangle_{\text{hole}}$, the magnetic flux density trapped in the cavity of the tube after field cooling in and removal of H_{cool}. The solid (dashed) curve is calculated including (neglecting) the contribution of the return flux of the magnetized grains which threads the cavity. (b) Data points display $\langle B_z \rangle_{\text{wall}}$, the magnetic flux trapped in the wall of the tube after removal of H_{cool}. The solid curve is theoretical and takes M_{gr} and H_{gr} into account as described in the text. Parameters for the calculations were $\mu_0 H_{*m} = \mu_0 I_c^*(0) = 1.1$ mT, $n = 0.5$ for matrix, $\mu_0 H_g^* = 12$ mT, $n = 0$ for grains, $C_{HM} = 0.45$, $f_g = 0.6$, and $f_m = 0.4$.

ined by many workers.[29–50]

The removal of H_{cool} and the to-and-fro swing of H_{cycle} induce an intergranular critical current I_c' to circulate azimuthally around the wall of the tube. To simplify the analysis we will assume throughout this paper that the intergranular critical current density $j_{cm}(r)$ is uniform along the length Z of the tube and varies only with the radial coordinate r. Thus we write

$$I_c' = I_c Z = Z \int_{R_i}^{R_o} j_{cm}(r)dr \ . \tag{3}$$

B. Monolithic homogeneous tube

Before we proceed to examine the complicated situation encountered in our work, where the tubes are finite in length and consist of weakly coupled high-critical-current-density grains, it is useful to outline the behavior for the simple idealized scenario, where the tube is infinitely long and homogeneous. Thus we first ignore the granular structure and neglect end effects.

The profiles of the magnetic field $H_m(r)$ which ensue from the H_{cool} and H_{cycle} procedures for this tube of idealized geometry and homogeneous composition are sketched in Fig. 5. Also, for simplicity, we consider surface barriers to entry or exit of magnetic flux to be negligible and take $B(r)=\mu_0 H(r)$, and hence let $H_{c1}=0$.

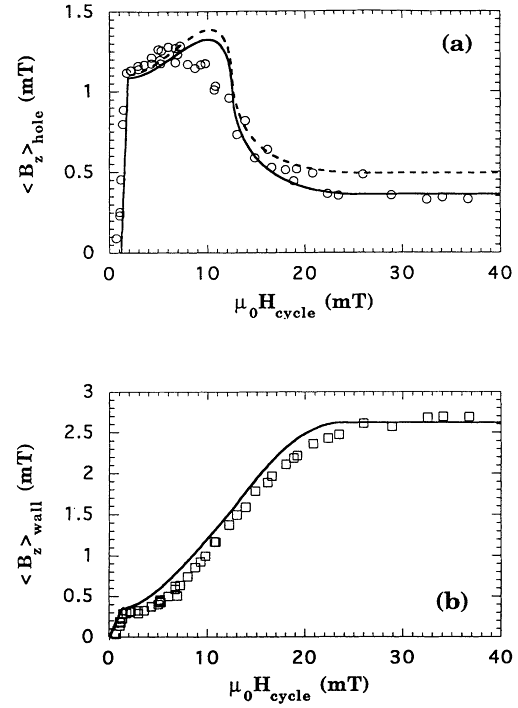

FIG. 2. YBCO tube at 77 K. (a) Data points are experimental and display $\langle B_z \rangle_{\text{hole}}$, after application and removal of H_{cycle}. The tube is zero-field cooled before each cycle. The solid (dashed) curve is calculated including (neglecting) the return flux of the magnetized grains returning through the cavity. (b) Data points display $\langle B_z \rangle_{\text{wall}}$ vs H_{cycle}. The solid curve is theoretical. Parameters used in the calculation are the same as listed in Fig. 1.

1. H_{cool} case

First we focus on the flux-trapping behavior in the low range where H_{cool} is less than a threshold value denoted H_{cool}^{*m}. Over this range of H_{cool}, all of the magnetic flux initially threading the cavity and permeating an annular volume of cross section

$$A_1=\pi(r_i^2-R_i^2) \tag{4}$$

remains undisturbed, and hence trapped, upon the removal of H_{cool} [see Fig. 5(a)]. The flux-retaining critical current I_c induced to circulate azimuthally by the removal of H_{cool} occupies the annular volume between r_i and R_o.

The position of the boundary r_i depends on $j_{cm}(r)$ and the magnitude of H_{cool} and migrates from R_o to R_i as H_{cool} approaches the threshold value H_{cool}^{*m}. From Ampère's law

$$\int \mathbf{H}\cdot d\mathbf{L}=I_{\text{enclosed}} \ , \tag{5}$$

we obtain

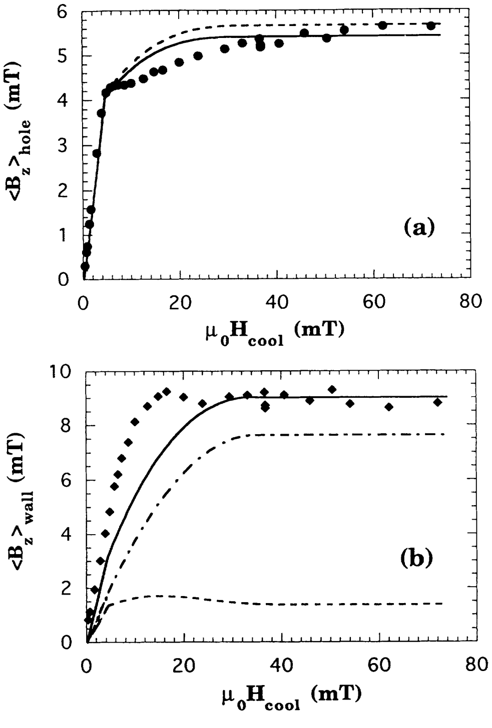

FIG. 3. BiSSCO tube at 77 K. (a) Data points are experimental and display $\langle B_z \rangle_{\text{hole}}$ after field cooling in and removal of H_{cool}. The solid (dashed) curve is calculated including (neglecting) the contribution of the return flux of the magnetized grains which threads the cavity. (b) Data points display $\langle B_z \rangle_{\text{wall}}$ after removal of H_{cool}. The three curves are theoretical. The dashed curve shows $f_m\langle H_m(r)\rangle$, the contribution of the matrix currents, and the dash-dot curve the net contribution of the magnetized grains (hence, $f_g M_{\text{gr}} - f_m C_{HM} M_{\text{gr}}$) to the total magnetic flux in the wall (solid curve). Parameters for the calculations were $\mu_0 H_{*m} = \mu_0 I_c^*(0) = 4.0$ mT, $\mu_0 H_g^* = 35$ mT, $n=1$ for the matrix, $n=0$ for the grains, $C_{HM}=0.16$, $f_g=0.5$, and $f_m=0.5$.

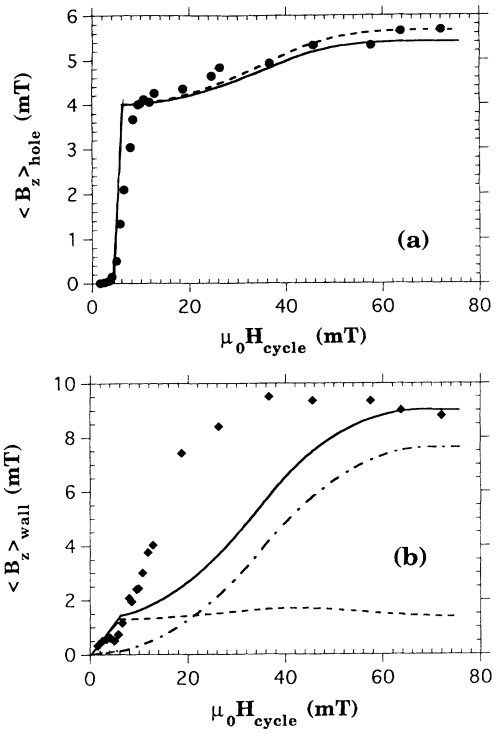

FIG. 4. BiSCCO tube at 77 K. (a) Data points display $\langle B_z \rangle_{\text{hole}}$, after application and removal of H_{cycle}. The tube is zero-field cooled before each cycle. The solid (dashed) curve is calculated including (neglecting) the contribution of the return flux of the magnetized grains which threads the cavity. (b) Data points display $\langle B_z \rangle_{\text{wall}}$ vs H_{cycle}. The three curves are theoretical. The dashed curve shows $f_m \langle H_m(r) \rangle$, the contribution of the matrix currents, and the dash-dot curve the net contribution of the magnetized grains (hence, $f_g M_{\text{gr}} - f_m C_{HM} M_{\text{gr}}$) to the total magnetic flux in the wall (solid curve). Parameters used in the calculations are the same as listed in Fig. 3.

$$\langle B_z \rangle_{\text{hole}} = \mu_0 H_{\text{cool}} = \mu_0 I_c \tag{6}$$

over the range $0 < H_{\text{cool}} \le H^{*m}_{\text{cool}}$.

When $H_{\text{cool}} \ge H^{*m}_{\text{cool}}$ is removed, the critical current I_c fills the entire cross section of the wall. We refer to this as a saturated critical state and let $I_c^*(0)$ denote I_c in these circumstances. Here the zero in parentheses indicates that magnetization of the grains is ignored since the wall is regarded as monolithic. Ampère's law then yields

$$\langle B_z \rangle^*_{\text{hole}} = \mu_0 H^{*m}_{\text{cool}} = \mu_0 I_c^*(0) \tag{7}$$

and $\langle B_z \rangle_{\text{hole}}$ traces a plateau for the range $H_{\text{cool}} \ge H^{*m}_{\text{cool}}$.

The evolution of $\langle B_z \rangle_{\text{hole}}$ and $\langle B_z \rangle_{\text{wall}}$ vs H_{cool} is displayed schematically in Fig. 5(c). The detailed structure of the rise of $\langle B_z \rangle_{\text{wall}}$ is determined by the dependence of j_{cm} on B. The ratio $\langle B_z \rangle_{\text{wall}} / \langle B_z \rangle_{\text{hole}}$ depends on r_i / R_o and the details of the profiles of $j_{cm}(r)$ hence $j_{cm}(B)$.

2. H_{cycle} *case*

During the application of H_{cycle} smaller than a threshold value denoted H^{*m}_{cycle}, magnetic flux penetrates into the wall but no flux enters the cavity [see Fig. 5(b)]. A critical current I_c opposing penetration of magnetic flux into the wall is induced to circulate azimuthally during the upsweep of H_{cycle}. This critical current occupies the annular volume between r_p and R_o when $H_{\text{cycle}} < H^{*m}_{\text{cycle}}$.

The position of the boundary r_p depends on $j_{cm}(r)$ and the magnitude of H_{cycle} and migrates from R_o to R_i as H_{cycle} approaches the threshold H^{*m}_{cycle}. From Ampère's law,

$$H^{*m}_{\text{cycle}} = I_c^*(0) = H^{*m}_{\text{cool}} \ . \tag{8}$$

Some of the flux which has entered the wall during the upsweep of H_{cycle} is released during its downsweep, as illustrated in Fig. 5(b). After the removal of $H_{\text{cycle}} \le H^{*m}_{\text{cycle}}$, two equal countercirculating critical currents I_{c1} and I_{c2} exist, where I_{c1} occupies the annular volume $r_p \le r \le r_i$ and I_{c2} the annular volume $r_i \le r \le R_o$.

For the monolithic, isotropic wall under consideration, the remanent $H_m(r)$ profiles are symmetric with respect to r_i when $H_{\text{cycle}} \le H^{*m}_{\text{cycle}}$, and hence

$$r_i = \frac{r_p + R_o}{2} \tag{9}$$

and

$$r_i = \frac{R_i + R_o}{2} \tag{10}$$

when $H_{\text{cycle}} = H^{*m}_{\text{cycle}}$.

For the intermediate range of H_{cycle} between the first penetration field H^{*m}_{cycle} and a second higher threshold field, denoted H^{**m}_{cycle}, the magnetic flux trapped in the cavity after the downsweep of H_{cycle} is determined by $j_{cm}(r)$ and the magnitude of H_{cycle} according to the expressions

$$\begin{aligned} \frac{\langle B_z \rangle_{\text{hole}}}{\mu_0} &= H_{\text{cycle}} - \int_{R_i}^{R_o} j_{cm1}(r)dr \\ &= \int_{r_i}^{R_o} j_{cm2}(r)dr - \int_{R_i}^{r_i} j_{cm1}(r)dr \\ &= I_{c2} - I_{c1} \ . \end{aligned} \tag{11}$$

H^{**m}_{cycle} is also referred to as the double penetration field since this field, applied to a "virgin" tube, would cause full penetration of flux across a wall of thickness $2(R_o - R_i)$.

Although the magnetic flux in the cavity and in the wall rises monotically as H_{cycle} is raised above H^{**m}_{cycle}, this additional flux is released during the downsweep of H_{cycle}. Consequently, in the higher-field range where $H_{\text{cycle}} > H^{**m}_{\text{cycle}}$, $\langle B_z \rangle_{\text{hole}}$ traces a plateau, where

$$\begin{aligned} \frac{\langle B_z \rangle_{\text{hole}}}{\mu_0} &= H^{**m}_{\text{cycle}} - \int_{R_i}^{R_o} j_{cm1}(r)dr \\ &= \int_{R_i}^{R_o} j_{cm2}(r)dr = I_c^*(0) = H^{*m}_{\text{cool}} \ . \end{aligned} \tag{12}$$

The evolution of $\langle B_z \rangle_{\text{hole}}$ vs H_{cycle} over these three regimes is displayed schematically in Fig. 5(d). The detailed structure of its rise from zero to the plateau is controlled by the dependence of j_{cm} on B. In the Bean approximation, where j_{cm} is taken independent of B, and hence is a constant, the rise of $\langle B_z \rangle_{\rm hole}$ vs $H_{\rm cycle}$ is linear over the range $H^{*m}_{\rm cycle} \le H_{\rm cycle} \le H^{**m}_{\rm cycle}$, and can be written

$$\frac{\langle B_z \rangle_{\rm hole}}{\mu_0} = H_{\rm cycle} - H^{*m}_{\rm cycle} = H_{\rm cycle} - I_c^*(0) \ . \qquad (13)$$

The evolution of $\langle B_z \rangle_{\rm wall}$ vs $H_{\rm cycle}$ is also illustrated in Fig. 5(d). The detailed structure of the S-shaped rise to the plateau is determined by the dependence of j_{cm} on B. The ratio $\langle B_z \rangle_{\rm wall} / \langle B_z \rangle_{\rm hole}$ at the plateau is the same as that for the $H_{\rm cool}$ procedure.

C. Granular multiply connected tubes

1. General framework

We now examine the effects of the magnetization of the grains of sintered materials on the density of trapped flux in the cavity and the wall of infinitely long tubes. The intergranular current can be regarded as circulating azimuthally along an intricate but continuous three-dimensional network or skeleton with a density denoted $j_{cm}(r)$. This network consists of the surface volume of grains and of the links and interfaces between the grains. The intergranular current occupies only a superficial portion of the volume of the grains, because the intragranu-

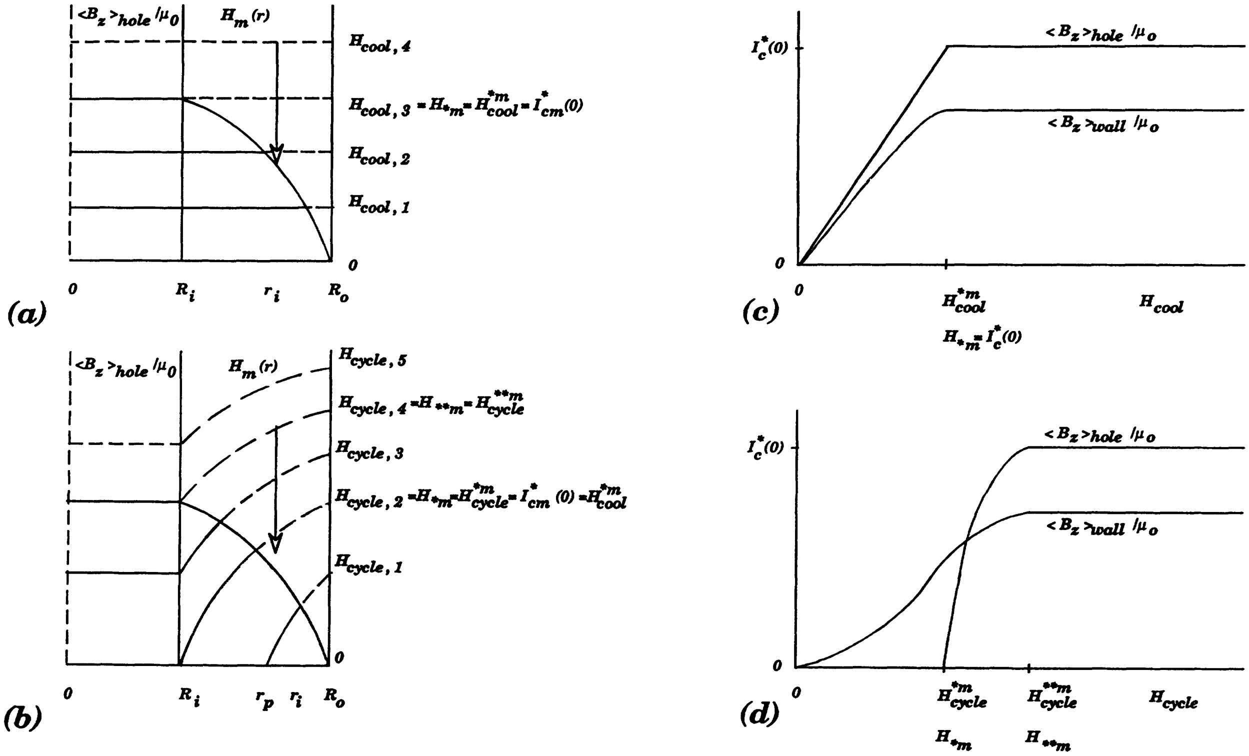

FIG. 5. Schematics for an infinitely long, homogeneous, (nongranular) tube. (a) The series of solid curves display $H(r)$, the remanent magnetic-field profiles in the wall and cavity of the tube after an axial $H_{\rm cool}$ of different intensities has been removed. The horizontal solid and dashed curves represent the profiles after field cooling (intrinsic Abrikosov diamagnetism is ignored, i.e., $H_{c1}=0$). $\langle B_z \rangle_{\rm hole}/\mu_0 = H_{\rm cool}$, when $H_{\rm cool} \le H_{*m}$. The initial $\langle B_z \rangle_{\rm hole}/\mu_0$ decreases to $H_{*m} = H^{*m}_{\rm cool} = I^*_{cm}(0)$, the saturated flux-retaining critical current (per unit length of the tube) when $H_{\rm cool} > H_{\rm cool,3} = H^{*m}_{\rm cool} = H_{*m}$ is removed. Thus the remanent $\langle B_z \rangle_{\rm hole}$ and $\langle B_z \rangle_{\rm wall}$ trace a plateau vs $H_{\rm cool} > H_{*m}$. (b) Schematic of initial and final $H(r)$ profiles with $H_{\rm cycle}$ of different intensities present (dashed curves) and after its removal (solid curves). The tube is zero-field cooled before each cycle. When $H_{\rm cycle} < H^{*m}_{\rm cycle}$, $\langle B_z \rangle_{\rm hole} = 0$ since the front of the initial field profile $r_p > R_i$, but magnetic flux is trapped in the wall. Flux enters the cavity when $H_{\rm cycle} > H_{\rm cycle,2} = H_{*m} = H^{*m}_{\rm cycle}$. Now, the initial and final $\langle B_z \rangle_{\rm hole}/\mu_0$ rises as $H_{\rm cycle}$ is augmented above H_{*m}. When $H_{\rm cycle} = H_{\rm cycle,4} = H_{**m} = H^{**m}_{\rm cycle}$ has been removed, the remanent profile is a duplicate of that encountered after the removal of $H_{\rm cool} = H_{\rm cool,3} = H_{*m} = H^{*m}_{\rm cool} = I^*_{cm}(0)$. Consequently, the remanent $\langle B_z \rangle_{\rm hole}$ and $\langle B_z \rangle_{\rm wall}$ trace a plateau of the same height as in (a) vs $H_{\rm cycle} > H_{**m}$. Also, we note that the remanent $H_m(r)$ profile is now the image of that initially existing at $H_{\rm cycle,2}$. (c) The evolution of $\langle B_z \rangle_{\rm hole}$ and $\langle B_z \rangle_{\rm wall}$ vs $H_{\rm cool}$ expected from (a). Note that $\langle B_z \rangle_{\rm hole} / \langle B_z \rangle_{\rm wall} > 1$ and the ratio at the plateaus is determined by the dependence of j_{cm} on B and by $(R_o - R_i)/(R_i + R_o)$. $\langle B_z \rangle_{\rm hole}$ is expected to rise linearly to its plateau but the details of the rise of $\langle B_z \rangle_{\rm wall}$ are determined by $j_{cm}(B)$ and its approach to its plateau is smooth. The thresholds of the two plateaus, denoted $H^{*m}_{\rm cool}$, are the same and correspond to $I_c^*(0) = H_{*m}$. Also, $\langle B_z \rangle_{\rm hole}/\mu_0 = I_c^*(0)$ at its plateau. (d) The evolution of $\langle B_z \rangle_{\rm hole}$ and $\langle B_z \rangle_{\rm wall}$ vs $H_{\rm cycle}$ expected from (b). Note that $\langle B_z \rangle_{\rm hole}$ rises above $\langle B_z \rangle_{\rm wall}$ when $H_{\rm cycle}$ is in the range between $H_{*m} = I_c^*(0)$ and H_{**m}. The height of the corresponding plateaus is the same as in (c). The ratio for the onset of the plateaus, $H^{**m}_{\rm cycle} / H^{*m}_{\rm cycle} = H_{**m}/H_{*m} = H_{**m}/I_c^*(0)$, and the "structure" of the rise of $\langle B_z \rangle_{\rm hole}$ and $\langle B_z \rangle_{\rm wall}$ are controlled by the dependence of j_{cm} on B. Further, $\langle B_z \rangle_{\rm hole}$ begins its rise when $H_{\rm cycle} = H^{*m}_{\rm cycle} = H_{*m} = H^{*m}_{\rm cool} = I^*_{cm}(0)$.

lar critical current density j_{cg} is orders of magnitude greater than j_{cm}.

It is useful to introduce the sponge analogy proposed decades ago by Mendelssohn[51,52] and Mendelssohn and Moore.[52] Now, however, we associate the body or matrix of the sponge with the intergrain network of weak critical current density j_{cm} and view the pores or voids of the sponge as filled by the interior volume of the grains capable of sustaining large critical current densities j_{cg}.

Now the removal of $H_{\rm cool}$ or the swing of $H_{\rm cycle}$ induces (a) a critical current I_c to circulate azimuthally around the tube through the network or "matrix" and (b) flux-shielding or flux-retaining persistent Ampèrian currents to circulate azimuthally around the periphery and the interior of the individual grains. Consequently, we can exploit the classical textbook treatment of a magnetized medium consisting of the juxtaposition of magnetic dipoles that consist of closed Ampèrian current loops. Let $\mathbf{M}_g$ denote the magnetization of decoupled grains viewed on a quasimacroscopic scale encompassing several grains. Although the grains are anisotropic and vary in size, shape, and orientation, the spatial average of the magnetization of an appropriate number of grains can be regarded as directed along the applied magnetic field. $\mathbf{M}_g$ may vary as a function of the radial coordinate r. Such a quasimacroscopic variation will arise when groups of grains have experienced different changes of ambient field, and hence possess a magnetization $\mathbf{M}_g$ which will differ in magnitude and perhaps also in polarity. In our work however, for simplicity, we will neglect these complications.

2. *Effect of $\mathbf{M}_g$ on the critical current in the wall*

Many workers have reported that the critical conduction current in granular high-T_c superconductors depends on the magnetic history of the specimen.[38–50] $I_{c\uparrow}$ when H_a has ascended after zero-field cooling is observed to be appreciably smaller than $I_{c\downarrow}$ in a corresponding H_a which has descended from a large value. Here the arrows ↑ and ↓ indicate that H_a has ascended or descended. This behavior has been attributed to the return field of the magnetized grains, which threads through the "matrix" or "sponge" where the intergrain current density $j_{cm}(r)$ is flowing. Let $H_g(r)$ denote the return field of the magnetized grains averaged over the dimension of the space between several grains. When H_a has ascended (descended), $H_g(r)$ of the diamagnetically (paramagnetically) magnetized grains is expected to aid (oppose) H_a. Consequently $j_{cm}(r)$ flows through a larger (smaller) total field

$$H_{\rm total}(r)=H_a \pm H_g(r) , \tag{14}$$

where the positive (negative) sign applies to H_a ascending (descending).

We now exploit this generally accepted model to examine the behavior of I_c^*, the saturation critical current induced to circulate circumferentially in the wall of the tubes of sintered type-II superconductors after removal of $H_{\rm cool}$ or $H_{\rm cycle}$. Since the grains are paramagnetically magnetized after removal of $H_{\rm cool}$, we write

$$H_{\rm total}(r)=H_m(r)-H_{\rm gr}(r) , \tag{15}$$

where $H_m(r)$ and $H_{\rm gr}(r)$ denote absolute values. Here, the subscript r is introduced to denote a remanent or residual $H_{\rm gr}(r)$. We note that $H_{\rm gr}(r)$ may be greater than $H_m(r)$ when the paramagnetic magnetization generated by the flux-retaining currents circulating inside the grains is strong.

To fix ideas and for simplicity we exploit dependences of the intergrain ("matrix") critical current density on $H_{\rm total}$ of the "standard" form,

$$j_{cm}(r)=\frac{\alpha}{\{H_{\rm total}(r)\}^n} . \tag{16}$$

We stress that $H_{\rm total}(r)$ denotes the absolute value, and hence

$$H_{\rm total}(r)=H_m(r)-H_{\rm gr}(r) \quad \text{when } H_m(r)>H_{\rm gr}(r) \tag{17a}$$

and

$$H_{\rm total}(r)=H_{\rm gr}(r)-H_m(r) \quad \text{when } H_{\rm gr}(r)>H_m(r) . \tag{17b}$$

For idealized (i.e., infinite) cylindrical tube geometry, Maxwell's equation $\nabla\times\mathbf{H}=\mathbf{j}$ together with the critical-state assumption reads

$$\frac{dH_m(r)}{dr}=-j_{cm}(r)=-\frac{\alpha}{\{H_{\rm total}(r)\}^n} . \tag{18}$$

Even in the idealized situation, where the grains are identical in size, shape, orientation, and composition, the magnetic moment of the grains, after removal of $H_{\rm cool}$ and $H_{\rm cycle}$, will generally vary with r. Indeed, the ensuing magnetization profile $M_g(r)$ will be uniform only if (i) the removal of $H_{\rm cool}$ and $H_{\rm cycle}$ extends over a sufficiently large range so as to induce a flux-retaining critical current density in the entire volume of all the grains, and (ii) the intragrain critical density is independent of B (i.e., obeys the Bean approximation where j_{cg} is a constant).

For simplicity, however, we will regard the final $M_g(r)$ profiles as spatially uniform. This simple picture will therefore become less valid when $H_{\rm cool}$ and $H_{\rm cycle}$ are not appreciable compared with H_{*m} and H_{**m}, respectively. Here H_{*m} and H_{**m} denote the first and double penetration fields across the wall of the tube when the magnetization of the grains plays a negligible role.

In this simple framework of uniform remanent $M_g(r)$ profiles, denoted $M_{\rm gr}$, we need to envisage only two regimes of behavior subsequent to the removal of $H_{\rm cool}$ or $H_{\rm cycle}$. In the "high"-field regime, $H_{\rm gr}$, the return flux associated with $M_{\rm gr}$, is larger in magnitude than $H_m(r)$ over the entire thickness of the wall [see Fig. 6(a)]. In the "low"-field regime, although assumed uniform, $H_{\rm gr}<H_m(r)$ over a volume $R_i \le r \le r_o$ and $H_{\rm gr}>H_m(r)$ over a volume $r_o \le r \le R_o$ [see Fig. 6(b)]; hence here two zones must be considered in the analysis.

First we consider the high-field (one-zone) regime. Introducing Eq. (17b) into (18) and regarding $H_{\rm gr}$ uniform

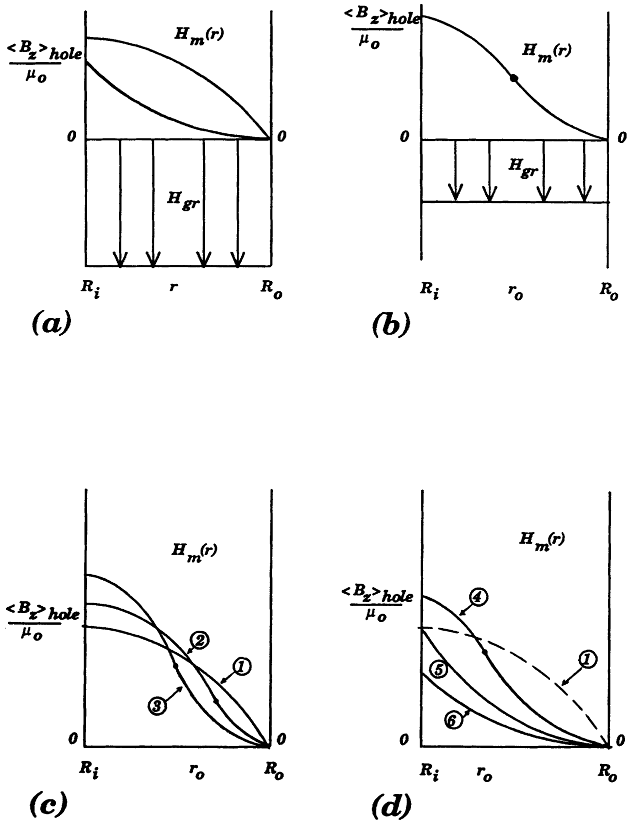

FIG. 6. Schematics of $H_m(r)$, the magnetic-field profiles generated in the matrix of a long tube of a weakly linked granular type-II superconductor by persistent currents of density $j_{cm}=\alpha/[H_{\text{total}}(r)]^n$ (where $n>0$), circulating azimuthally in the matrix around the axis of the tube after removal of $H_{\text{cool}}\geq H_{*m}=I^*_{cm}(0)$ or $H_{\text{cycle}}\geq H_{**m}$ [Eqs. (20) and (28)]. In every case, $\langle B_z\rangle_{\text{hole}}/\mu_0=H_m(R_i)$ and $H_m(R_o)=0$. In (a) and (b) the grains magnetized by the removal of H_{cool} and H_{cycle} generate a return field H_{gr} in the matrix which is directed opposite to $H_m(r)$; hence $H_{\text{total}}(r)=H_{\text{gr}}-H_m(r)$ in the region $r_o\leq r\leq R_o$ and $H_{\text{total}}(r)=H_m(r)-H_{\text{gr}}$ in the region $R_i\leq r\leq r_o$. For simplicity, $H_{\text{gr}}=C_{HM}M_{\text{gr}}$ is taken uniform and the parameter C_{HM} is taken independent of M_{gr}, the remanent magnetization of the grains. The evolution of M_{gr} vs H_{cool} and H_{cycle} is developed in Appendix A. M_{gr} and H_{gr} attain saturation values M^*_{gr} and H^*_{gr} at the plateaus of $\langle B_z\rangle_{\text{hole}}$ and $\langle B_z\rangle_{\text{wall}}$ vs H_{cool} and H_{cycle}. For our YBCO tube and that of Yunhui Xu (Ref. 3), $H^*_{\text{gr}}\gg H_{*m}=I^*_{cm}(0)$ and the plateaus correspond to the lower curves depicted in (a). In these specimens, the profiles evolve from that labeled (1) through (6) in (c) and (d) as H_{cool} and H_{cycle} are augmented. Consequently, $\langle B_z\rangle_{\text{hole}}$ displays a prominent peak which then descends to a plateau. The lower profile shown in (a) also corresponds to the observation of Eberhardt, Hibbs, and Campbell (Ref. 4) that the flux-retaining persistent current appears to be concentrated in the vicinity of R_i instead of R_o. (We note that $j_{cm}=-dH_m/dr$.) In our BiSSCO tube and the specimens studied by Willis *et al.* (Ref. 1) and Jingrong Wang *et al.* (Ref. 2), $H^*_{\text{gr}}\approx H_{*m}/(2)^{1/(n+1)}$, hence the $H_m(r)$ profile displayed in (b) is encountered at the plateau of $\langle B_z\rangle_{\text{hole}}/\mu_0=I^*_c$. In these specimens, $H_m(r)$ evolves only from the curve labeled (1) through (2) to (3) as H_{cool} and H_{cycle} are augmented.

leads to

$$\begin{aligned}-\int_r^{R_o}[H_{\text{gr}}-H_m(r)]^n dH_m(r)&=\int_r^{R_o}[H_{\text{gr}}-H_m(r)]^n d\{H_{\text{gr}}-H_m(r)\}\\&=\alpha\int_r^{R_o}dr\ .\end{aligned}\tag{19}$$

Upon integration, and noting that $H_m(R_o)=0$, since H_{cool} and H_{cycle} have been removed, this yields

$$H_m(r)=H_{\text{gr}}-\left\{H_{\text{gr}}^{n+1}-H_{*m}^{n+1}\frac{(R_o-r)}{(R_o-R_i)}\right\}^{1/(n+1)}\ ,\tag{20}$$

where

$$H_{*m}^{n+1}=\alpha(n+1)(R_o-R_i)=[I^*_c(0)]^{n+1}\tag{21}$$

and

$$I^*_c(0)=H_{*m}=\langle B_z\rangle^*_{\text{hole}}/\mu_0\tag{22}$$

are the critical current, the penetration field, and the magnetic field trapped in the tube when the grains are not magnetized. The magnetic field in the cavity is then given by

$$\begin{aligned}\frac{\langle B_z\rangle_{\text{hole}}}{\mu_0}&=H_m(R_i)\\&=H_{\text{gr}}-\{H_{\text{gr}}^{n+1}-H_{*m}^{n+1}\}^{1/(n+1)}\\&=H_{\text{gr}}-\{H_{\text{gr}}^{n+1}-[I^*_c(0)]^{n+1}\}^{1/(n+1)}\ .\end{aligned}\tag{23}$$

Combining Eqs. (17b), (18), and (20), we note that the current density j_{cm} is largest along the inner surface of the tube. This corresponds to the result reported by Eberhardt, Hibbs, and Campbell[4] who offer no explanation for this observation. In our model, this distribution occurs because the total magnetic field in the matrix is weakest along R_i when the grains carry a saturation paramagnetic magnetization.

In the low-field regime, Eq. (20) also describes $H_m(r)$ in the outer zone, $r_o\leq r\leq R_o$, where, although assumed uniform, $H_{\text{gr}}>H_m(r)$. At the boundary r_o between the outer and inner zones,

$$H_m(r)=H_m(r_o)=H_{\text{gr}}\tag{24}$$

since, here, $H_{\text{total}}(r)=H_m(r)-H_{\text{gr}}(r)=0$. Hence from Eq. (20) we obtain

$$\frac{R_o-r_o}{R_o-R_i}=\left\{\frac{H_{\text{gr}}}{H_{*m}}\right\}^{n+1}\ ,\tag{25}$$

which describes the migration of the zone boundary r_o from R_o to R_i as H_{gr} is made to increase in magnitude from zero to H_{*m}. We note that the maximum matrix current density $j_{cm}(r)$ is encountered along the zone boundary $r=r_o$. In the limit of zero magnetization of the grains, $H_{\text{gr}}=0$, then $r_o=R_o$, and thus the outer zone vanishes and the maximum matrix current now appears along the outer radius.

For the inner zone where, although assumed uniform, $H_{\text{gr}}<H_m(r)$, introducing Eq. (17a) into Eq. (18) leads to

$$\int_r^{r_o}[H_m(r)-H_{\rm gr}]^n dH_m(r)$$

$$=\int_r^{r_o}[H_m(r)-H_{\rm gr}]^n d\{H_m(r)-H_{\rm gr}\}$$

$$=-\alpha\int_r^{r_o}dr \ . \qquad (26)$$

Integrating and noting again that $H_{\rm gr}=H_m(r_o)$ since $H_{\rm total}=0$ at $r=r_o$, this yields

$$H_m(r)=H_{\rm gr}+H_{*m}\left\{\frac{(r_o-r)}{(R_o-R_i)}\right\}^{1/(n+1)} , \qquad (27)$$

which applies over the volume $R_i \le r \le r_o$. Introducing Eq. (25), this reads

$$H_m(r)=H_{\rm gr}+\left\{H_{*m}^{n+1}\frac{(R_o-r)}{(R_o-R_i)}-H_{\rm gr}^{n+1}\right\}^{1/(n+1)} . \qquad (28)$$

Consequently, for the "low-field" regime, we find from Eq. (28) that

$$\frac{\langle B_z\rangle_{\rm hole}}{\mu_0}=H_m(R_i)$$

$$=H_{\rm gr}+\{H_{*m}^{n+1}-H_{\rm gr}^{n+1}\}^{1/(n+1)}$$

$$=H_{\rm gr}+\{[I_c^*(0)]^{n+1}-H_{\rm gr}^{n+1}\}^{1/(n+1)} . \qquad (29)$$

As required, $\langle B_z\rangle_{\rm hole}/\mu_0=H_{*m}=I_c^*(0)$, when the grains are not magnetized, and hence $H_{\rm gr}=0$.

The dashed curves in (a) of Figs. 1–4 were obtained using Eqs. (23) and (29). The linear rise of $\langle B_z\rangle_{\rm hole}$ vs $H_{\rm cool}$ over the range $0<H_{\rm cool}\le I_c^*(0)=H_{*m}$ is independent of the magnetization of the grains for the infinitely long tube [see Figs. 5(a) and 5(c)]. For the $H_{\rm cycle}$ procedure we ignore the effect of $M_{\rm gr}$ on (i) the threshold for first penetration of flux into the cavity and (ii) the structure of the rapid rise of $\langle B_z\rangle_{\rm hole}$ vs $H_{\rm cool}$ in the range of $H_{\rm cycle}^{*m}\le H_{\rm cycle}\le H_{\rm cycle}^{**m}$ [see Figs. 5(b) and 5(d)], since the assumption of a uniform $M_g(r)$ is not valid in this range.

It is remarkable that the simple model which leads to Eqs. (23) and (29) qualitatively and quantitatively reproduces the two very different modes of flux-trapping behavior displayed by the YBCO and BiSCCO tubes. Indeed, these two equations predict a wide "spectrum" of flux-trapping behavior. It is useful to identify the key elements in this model which control the resulting variety of behavior.

The crucial parameters which control the resulting variety of behavior are the relative magnitudes of

(i) H_{*m}, the first penetration field across the wall of the tube,

(ii) H_{*g}, the first penetration field into the grains, and

(iii) $H_{\rm gr}^*$, the return field in the matrix at $M_{\rm gr}^*$, the saturation remanent magnetization of the grains.

The first of these three parameters characterizes the matrix, the second characterizes the grains, and the third is determined by the structure of the grain-matrix mosaic. H_{*m} will depend on the thickness of the wall, the intergrain (matrix) critical current density j_{cm}, and its dependence on magnetic flux density. H_{*g} will depend on some "effective" dimension of the idealized average grain, the intragrain critical current density j_{cg}, and its dependence on magnetic flux density. For grains of simple idealized geometries and standard dependences of j_{cg} on B, we can readily calculate the ratio $M_{\rm gr}/H_{*g}$, as shown in Appendix A.

The development of a relationship between the return field inside the matrix and the magnetization of the grains is a formidable challenge.[29–34,53–64] We assume, for simplicity, that the ratio of the return field $H_{\rm gr}$ to the corresponding grain magnetization $M_{\rm gr}$ does not vary appreciably as $M_{\rm gr}$ is varied. Consequently, we take

$$\frac{H_{\rm gr}}{M_{\rm gr}}=\frac{H_{\rm gr}^*}{M_{\rm gr}^*}=C_{HM} , \qquad (30)$$

where C_{HM} is a constant for a given specimen and fixed temperature. Thus C_{HM} serves as the adjustable parameter for modeling the flux-trapping behavior of a specific tube.

The critical-state model is taken to dictate the evolution of $M_{\rm gr}$ as a function of $H_{\rm cool}$ and $H_{\rm cycle}$. This evolution is developed in Appendix A for simple idealized geometries and various dependences of j_{cg} on B. This analysis shows that the curves of $M_{\rm gr}$ vs $H_{\rm cool}$ and $H_{\rm cycle}$ are "generic," that is, not sensitive to the choice of geometry or of dependence of j_{cg} on B when the pertinent quantities are normalized with respect to $M_{\rm gr}^*$ and H_{*g}.

In the calculations of $\langle B_z\rangle_{\rm hole}$ vs $H_{\rm cool}$ and $H_{\rm cycle}$ using Eqs. (23) and (29) we have exploited the simplest expressions for $M_{\rm gr}$ from Appendix A, namely, that where the grains have idealized slab geometry and the intragrain critical current density is independent of B, hence $j_{cg}=\alpha_B$ (i.e., the Bean approximation). Good agreement with observations is obtained taking the adjustable parameter $C_{HM}=H_{\rm gr}/M_{\rm gr}=0.16$ and 0.45 for the BiSCCO and YBCO tubes respectively.

The evolution of the $H_m(r)$ profiles generated by Eqs. (20) and (28) when applied to the YBCO tube is illustrated in Figs. 6(c) and 6(d). Here $H_{\rm gr}^*\approx 2.3H_{*m}$, and hence the entire spectrum of profiles displayed in these two figures is encountered as the augmentation of $H_{\rm cool}$ and $H_{\rm cycle}$ causes the remanent magnetization of the grains $M_{\rm gr}$ to grow to the saturation level $M_{\rm gr}^*$.

$\langle B_z\rangle_{\rm hole}=\mu_0H_m(R_i)$ first rises to a peak vs $H_{\rm cool}$ and $H_{\rm cycle}$ as the $H_m(r)$ profiles are made to evolve from that labeled (1) through (2) to (3) in the sketches of Fig. 6(c). The summit of the peak is attained when

$$H_{\rm gr}=(\tfrac{1}{2})^{1/(n+1)}H_{*m}=(\tfrac{1}{2})^{1/(n+1)}I_c^*(0) , \qquad (31)$$

which follows from Eq. (29), and solving for $dH_m(R_i)/dH_{\rm gr}=0$. At the summit,

$$\frac{\langle B_z\rangle_{\rm hole}}{\mu_0}=I_{c,\max}^*=2^{n/(n+1)}I_c^*(0)=2^{n/(n+1)}H_{*m} , \qquad (32)$$

which follows from introducing Eq. (31) into Eq. (29). The summit is encountered when $H_{\rm total}(r)=0$ at the midradius

$$R_m = \frac{R_i + R_o}{2} , \tag{33}$$

and hence $H_{\text{gr}} = H_m(r)$ at $r = R_m$. The saturated circumferential matrix current is maximized in these circumstances.

For the YBCO tube, the descent from the summit is traced as further augmentation of H_{cool} and H_{cycle}, and hence of H_{gr}, causes the $H_m(r)$ profiles to evolve beyond that labeled (3) in the sketches of Figs. 6(c) and 6(d). The plateau is attained when H_{cool} and H_{cycle} are sufficiently large so that their removal generates M_{gr}^*, the saturation remanent magnetization of the grains and the corresponding saturation value, and hence maximum value, $H_{\text{gr}} = H_{\text{gr}}^*$. The remanent $H_m(r)$ profile for the YBCO tube is then "frozen" in a configuration represented by the curve labeled (6) in Fig 6(d). The removal of H_{cool} of magnitudes greater than $(H_g^* + H_{*m})$ and of H_{cycle} greater than $(H_g^{**} + H_{*m})$ causes no further increase of M_{gr} and H_{gr} and hence no changes in the resulting $H_m(r)$ profile and no further decline in

$$H_m(R_i) = I_c^*(H_{\text{gr}}^*) = \langle B_z \rangle_{\text{hole}} / \mu_0 \, .$$

Consequently, a plateau is now observed in the latter quantity as a function of H_{cool} and H_{cycle}. The corresponding remanent $\langle B_z \rangle_{\text{wall}}$ also ceases to evolve with H_{cool} and H_{cycle} and also traces a plateau.

For the BiSCCO tube, the saturation remanent magnetization of the grains is attained when $H_{\text{gr}}^* \approx 0.707 H_{*m}$, which is in marked contrast to the situation encountered with the YBCO tube where $H_{\text{gr}}^* \approx 2.3 H_{*m}$. As a consequence, the saturated remanent $H_m(r)$ profiles in the BiSCCO tube evolve from the low-applied-field configuration labeled (1) through that labeled (2) in Fig. 6(c), but "terminate" or "freeze" at a configuration like that labeled (3). The configurations of the $H_m(r)$ profiles in Fig. 6(d) are not generated because M_{gr}^*, the saturation magnetization of the grains, and hence $H_{\text{gr}} = H_{\text{gr}}^*$, are already attained when configuration (3) of Fig. 6(c) is established. Therefore the plateaus of $\langle B_z \rangle_{\text{hole}}$ vs H_{cool} and H_{cycle} are traced with $\langle B_z \rangle_{\text{hole}}$ at or in the vicinity of its maximum value.

According to our model this is also the situation which prevails in the observations of $\langle B_z \rangle_{\text{hole}}$ vs H_{cycle} reported by Willis *et al.*[1] and Jingrong Wang *et al.*[2] on YBCO tubes at 75 and 78 K, respectively. These workers observe a plateau for $\langle B_z \rangle_{\text{hole}}$ where the ratio $I_{c,\max}^* / H_{*m} \approx 2.0$ and 1.8, respectively. (We note that the quantity they denote H_{sh} corresponds to our H_{*m}.)

As illustrated in Fig. 7, the large enhancement of $\langle B_z \rangle_{\text{hole}} / \mu_0$ with respect to H_{*m} observed by Willis *et al.*[1] and Jingrong Wang *et al.*[2] can be reproduced by increasing the sensitivity of j_{cm} to H. This is readily achieved by choosing a large value for n in the prescription $j_{cm} = \alpha / H_{\text{total}}^n$ and hence in Eq. (32). Alternatively, as shown in Appendix B, this can be accomplished by choosing appropriate values for the parameters j_{c0} and H_0 in the prescription $j_{cm} = j_{c0} e^{-H/H_0}$. We note that $I_{c,\max}^* / H_{*m} = 2$ is the maximum enhancement ratio predicted by our model for both prescriptions for $j_{cm}(H)$.

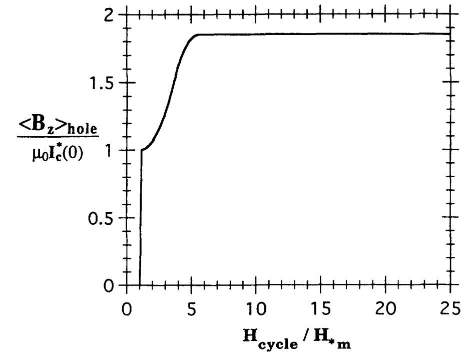

FIG. 7. Behavior generated by our model [Eq. (29)] for $\langle B_z \rangle_{\text{hole}}$, the magnetic field trapped in the cavity of a long tube of a weak-link granular type-II superconductor vs H_{cycle} for specimens where the matrix current density j_{cm} is rapidly decreasing with B and the saturation return field in the matrix $H_{\text{gr}}^* \approx H_{*m} / (2)^{1/(n+1)} \approx 0.93 H_{*m}$. Both $\langle B_z \rangle_{\text{hole}} / \mu_0$ and H_{cycle} are normalized to the initial shielding field $H_{*m} = I_c^*(0)$. This theoretical curve should be compared with the data of Willis *et al.*[1] (their Fig. 2) and the data of Jingrong Wang *et al.*[2] (their Fig. 3). Here, $j_{cm} = \alpha / [H_{\text{total}}(r)]^n$ with $n = 8$, $H_{*g} = 2.5 H_{*m}$, and $C_{HM} = 0.75$, and H_{grh} is ignored since k_d is negligible [our Eq. (42)]. M_{gr} vs H_{cycle} is taken from Appendix A for a thin-slab grain where j_{cg} is a constant (Bean approximation).

Yunhui Xu[3] reports flux-trapping behavior in the cavity of a hollow tube of YBCO at 77 K very similar to that exhibited by our YBCO tube. To illustrate the versatility and validity of our model we display theoretical curves in Fig. 8 which reproduce his observations in the format he employed in his Fig. 3. In these calculations we introduce the dimensions and properties [i.e., $H_{*m} = I_c^*(0)$] of his specimens.

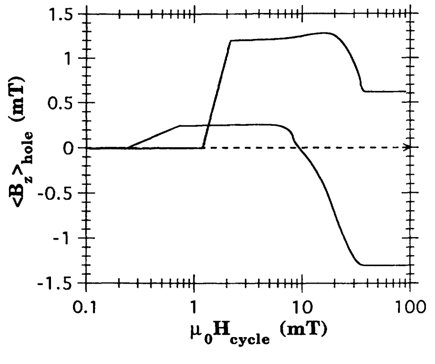

FIG. 8. Behavior generated by our model [Eqs. (23), (29), and (42)] for the two YBCO tubes studied by Yunhui Xu (Ref. 3). These two theoretical curves are displayed in the same format he used and should be compared with his corresponding data displayed in his Fig. 3. The dimensions of his long and short tubes lead to $k_d = 0.12$ and 0.29 [see our Eq. (42)] and his data indicate that the trapping fields $\mu_0 H_{*m} = \mu_0 I_c^*(0) = 1.2$ and 0.25 mT, respectively. Hence these quantities were used in our calculations for our upper and lower curves, respectively. For both theoretical curves we took $j_{cm} = \alpha / [H_{\text{total}}(r)]^{1/2}$, $H_{*g} = 18$ mT, $f_g = f_m = 0.5$, and M_{gr} vs H_{cycle} (from Appendix A) for a thin-slab grain where j_{cg} is uniform (Bean approximation). We let the adjustable parameter $C_{HM} \equiv H_{\text{gr}}^* / M_{\text{gr}}^* = 0.30$ and 0.136 for the long and short tube, respectively.

3. *Effect of* M_{gr} *on* $\langle B_z \rangle_{\mathrm{wall}}$

An inspection of the data displayed in Figs. 1–4 reveals that the remanent magnetic flux density trapped in the wall of the tubes rises appreciably above that trapped in the cavity. This feature is opposite to the behavior expected for a tube with a homogeneous (nongranular) wall and illustrated in Figs. 5(c) and 5(d). The fact that $\langle B_z \rangle_{\mathrm{wall}}$ rises well above $\langle B_z \rangle_{\mathrm{hole}}$ provides clear evidence that j_{cg}, the critical density of the persistent currents induced to circulate inside the grains by the removal of H_{cool} or H_{cycle}, is much larger than j_{cm}, the critical current density in the matrix. As a consequence, the grains trap a larger remanent magnetic flux density in their interior than can be trapped by the matrix alone.

The values of H_{cool} and H_{cycle} for the onset of the plateaus observed in the locus the $\langle B_z \rangle_{\mathrm{hole}}$ and $\langle B_z \rangle_{\mathrm{wall}}$ in Figs. 1–4 provide a direct measure of H_{*g} and H_{**g}, the first and the double penetration fields into the grains. Further, the ratio H_{**g}/H_{*g} yields information on the dependence of j_{cg} on B in the low-field range.

Our simple model also qualitatively and quantitatively accounts for the behavior of $\langle B_z \rangle_{\mathrm{wall}}$, the magnetic flux density trapped inside the wall of the tubes after the removal of H_{cool} and H_{cycle}. We can write

$$\frac{\langle B_z \rangle_{\mathrm{wall}}}{\mu_0} = f_g M_{\mathrm{gr}} - f_m H_{\mathrm{gr}} + f_m \langle H_m(r) \rangle \ , \tag{34}$$

applicable when $H_{\mathrm{cool}} > H_{*m}$ and $H_{\mathrm{cycle}} > 2^{1/(n+1)} H_{*m}$. Here, f_g is the fraction of the volume of the wall occupied by the grains. Since $H_m(r)$ and H_{gr} both permeate the matrix network supporting j_{cm} and the voids, we require that

$$f_g + f_m = 1 \ . \tag{35}$$

Since the return magnetic flux cannot exceed the remanent flux trapped in the grains, the choice of f_g and the parameter C_{HM} must satisfy the condition that

$$f_g M_{\mathrm{gr}} > f_m H_{\mathrm{gr}} = f_m C_{HM} M_{\mathrm{gr}} = (1 - f_g) C_{HM} M_{\mathrm{gr}} \ . \tag{36}$$

For simplicity, we consider f_g and hence f_m independent of B over the range of B under consideration. Our approach is equivalent to that exploited by many workers who choose to introduce an effective permeability as the adjustable parameter in the treatment of $\langle B \rangle$ versus the history of the applied field H_{cool} and H_{cycle}.

$\langle H_m(r) \rangle$, the spatial average of the magnetic field generated by the circumferential matrix current, can be written

$$\langle H_m(r) \rangle = \frac{2}{(R_o^2 - R_i^2)} \int_{R_i}^{R_m} H_m(r) r \, dr \ . \tag{37}$$

This definition assumes that the matrix fills the entire volume of the wall. Following standard practice this average is "corrected" by introducing a field-independent factor $f_m < 1$ in Eq. (34).

Introducing Eqs. (20) and (28) into Eq. (37), the evolution of $\langle H_m(r) \rangle$ vs $H_{\mathrm{gr}} = C_{HM} M_{\mathrm{gr}}$ is calculated using the same expression for M_{gr} vs H_{cool} and H_{cycle} employed earlier and developed in Appendix A. The crucial feature which emerges from this analysis and is illustrated in Appendix C is that the locus of $\langle H_m(r) \rangle$ vs H_{gr} (and hence vs M_{gr}) traces a peak. For a thin-walled tube, where $n=1$, this summit is attained when

$$H_{\mathrm{gr}} = H_{\mathrm{gr}}^{*} = \left[\frac{1}{2} - \frac{\sqrt{2}}{4} \right]^{1/2} H_{*m} = 0.383 H_{*m} \ , \tag{38}$$

and hence well before the corresponding locus of $\langle B_z \rangle_{\mathrm{hole}}$ has reached its summit. Consequently, the contribution of, $\langle H_m(r) \rangle$ to $\langle B_z \rangle_{\mathrm{wall}}$ traces a peak while the component associated with M_{gr} monotonically rises to a plateau as a function of H_{cool} and H_{cycle}. These contributions are displayed separately and in combination in Figs. 1–4. In these calculations we have taken $f_g = f_m = 0.5$ for the BiSSCO tube and $f_g = 0.6, f_m = 0.4$ for the YBCO tube.

4. *Effect of finite geometry*

In the foregoing we have exploited idealized geometry and hence regarded the length L of the tube to be large compared with the outer diameter D_o. The situation for "short" tubes is considerably more complicated. First, Maxwell's equation $\nabla \times \mathbf{H} = \mathbf{j}$ together with the critical-state assumption that $\mathbf{j} = \mathbf{j}_{cm}(H)$ now reads

$$j_{cm} = \frac{\partial H_r}{\partial z} - \frac{\partial H_z}{\partial r} \ . \tag{39}$$

Hence, the $H_m(r)$ profiles and related formulas developed above must be regarded as approximations which become less appropriate as the aspect ratio L/D_o diminishes. Further, now a fraction of the return flux of the magnetized grains threads the cavity of the tube. Let H_{grh} denote the spatial average of this return magnetic field threading the midplane of the cavity. To obtain an estimate of H_{grh} we continue to regard M_{gr} as uniform over the volume of the wall. Consequently $\nabla \times \mathbf{M} = \mathbf{0}$ and the basic textbook formula

$$\mathbf{K}_{gs} = f_g \mathbf{M}_g \times \hat{r} \ , \tag{40}$$

where r is a unit radial vector, and the "filling" factor f_g is explicitly taken into account, leads to the simple results that

$$\mathbf{K}_{gs}(R_o) = \hat{\phi} f_g M_g = -\mathbf{K}_{gs}(R_i) \ . \tag{41}$$

Here, K_{gs} is an equivalent (pseudo-) surface current flowing along the inner and outer circumferences of the wall of the tube. K_{gs} arises from localized currents confined to circulate within the individual grains, but their juxtaposition is viewed as equivalent to a continuous current flowing circumferentially along the inner and outer boundaries of the wall. The collection of magnetized grains in the wall is then replaced by two "thin" solenoids of equal length L, carrying countercirculating currents of equal magnitude $K_{gs} = f_g M_g$ per unit length of the tube.

Introducing Eq. (41) into the formula for thin solenoids of finite length, the resulting return magnetic field at the center of the tube reads

$$H_{\text{grh}} = -f_g M_g \left\{ \frac{L}{\sqrt{D_i^2+L^2}} - \frac{L}{\sqrt{D_o^2+L^2}} \right\}$$
$$= -k_d f_g M_g \ , \qquad (42)$$

applicable when $H_{\text{cool}} > H_{*m}$ and $H_{\text{cycle}} > 2^{1/(n+1)} H_{*m}$. Here the negative sign in front of the curly brackets indicates that H_{grh} is directed opposite to the magnetization of the grains. For the YBCO and BiSCCO tubes, $k_d = 0.10$ and 0.028 respectively. The solid curves in part (a) of Figs. 1–4 display the results calculated when H_{grh} [Eq. (42)] is taken into account. For the very short YBCO tube studied by Yunhui Xu,[3] this return field is the dominant contribution to $\langle B_z \rangle_{\text{hole}}$. The lower curve in Fig. 8 displays our calculation of $\langle B_z \rangle_{\text{hole}}$ vs H_{cycle} for his short specimen, exploiting our model and the parameters listed in the figure caption.

IV. SUMMARY AND CONCLUSION

We have reported on measurements of $\langle B_z \rangle_{\text{hole}}$ and $\langle B_z \rangle_{\text{wall}}$, the remanent magnetic flux density trapped at 77 K in the cavity and the wall of tubes of two different weakly coupled granular high-T_c superconductors of different aspect ratios. The magnetic flux was trapped using two standard procedures denoted H_{cool} and H_{cycle}. The data curves for $\langle B_z \rangle_{\text{hole}}$ vs H_{cool} and H_{cycle} exhibit dramatically different behaviors for the two materials. Examples of both modes of behavior have already been reported in the literature.[1–3,5]

We exploit the prevailing concept that some of the return flux of the magnetized grains threads the continuous intergrain matrix or network and affects I_c, the circumferentially circulating critical current which this matrix can support. We assume for simplicity that H_{gr}, the spatial average of this return flux in the volume of the matrix, is uniform and proportional to M_{gr}, the remanent magnetization of the grains. The variation of M_{gr} vs H_{cool} and H_{cycle} is developed in Appendix A in the framework of the critical-state model for idealized grain geometries and standard dependences of the intragrain critical current density j_{cg} on B.

The critical-state concept is also exploited to derive simple expressions for $H_m(r)$, the profile of the magnetic field permeating the matrix of infinitely long tubes after removal of H_{cool} and H_{cycle}. These expressions generate a spectrum of behavior for $\langle B_z \rangle_{\text{hole}} = \mu_0 H_m(R_i)$ vs H_{cool} and H_{cycle}, and satisfactorily describe our observations for $\langle B_z \rangle_{\text{hole}}$ as well as the data reported by other workers.[1–3,5,19] The model also accounts for the feature noted by Eberhardt, Hibbs, and Campbell[4] that the current density supporting the trapped flux in their measurements exhibited a maximum near the inner radius rather than along the outer radius as they expected.

A significant fraction of the return field of the magnetized grains will thread the cavity of short tubes and is denoted H_{grh}. Assuming M_{gr} to be uniform over the volume of the wall, we estimate H_{grh} at the center of the cavity and take the effect of this component into account in weakening the magnetic field trapped in the cavity of our YBCO tube. This contribution is shown to play a major role in the flux-trapping behavior of the very short (i.e., annular) YBCO tube studied by Yunhui Xu.[3]

Introducing a parameter f_g, the fraction of the wall volume occupied by the grains, we also apply our simple model to the successful description of the evolution of $\langle B_z \rangle_{\text{wall}}$ vs H_{cool} and H_{cycle}. We note that the model "predicts" the appearance of a "hump" in these curves. This feature is evident in our data for the BiSCCO tube.

Our model provides a simple, self-consistent framework for estimating (i) H_{*g} and H_{**g}, the first and double penetration fields into the grains, (ii) the dependence of the intragrain critical current density j_{cg} on B in the low-field range, (iii) the dependence of j_{cm}, the critical current density in the matrix, on B in the low-field range, and (iv) the magnitude, inside the matrix, of the return flux of the magnetized grains from data on $\langle B_z \rangle_{\text{hole}}$ vs H_{cool} and H_{cycle}. The volume fraction of the grains, and hence of the matrix, can be estimated from the corresponding data on $\langle B_z \rangle_{\text{wall}}$.

ACKNOWLEDGMENTS

The authors are indebted to Dr. Vladimir Plechácek and the Academy of Science of the Czech Republic for providing BiSSCO tubes and to Dr. Martin P. Maley and the Los Alamos National Laboratory for providing an YBCO tube.

APPENDIX A

For completeness, we develop expressions for the remanent magnetic flux density trapped in isotropic grains of idealized geometry by the H_{cool} and H_{cycle} procedures. We consider a specimen (a grain) of uniform rectangular cross section $4ab$. The homogeneous applied magnetic field H_a and the infinite length of the specimen are directed along the z axis. We neglect surface barriers and reversible Abrikosov diamagnetism, and hence let $H = B/\mu_0$.

Some special cases of these results have been published earlier.[65,66] To scan the expected behavior we display curves for infinite slab and cylinder geometry for two standard but very different dependences of the critical current density j_c on B, namely the simple Bean and Kim approximations where

$$j_c = \alpha_B \text{ and } j_c = \frac{\alpha_K}{H} \ , \qquad (\text{A1})$$

where α_B and α_K are temperature-dependent parameters characterizing the specimen.

The field-shielding and flux-retaining critical currents circulate in concentric rectangular loops in the x-y planes with a current density

$$|\pm\hat{x} j_x| = |\pm\hat{y} j_y| = j_c \ , \qquad (\text{A2})$$

which is uniform along a loop whose sides situated at $\pm x_1$ and $\pm y_1$ are equidistant from the boundaries $x = \pm a$ and $y = \pm b$ of the specimen. A quarter of such a loop, where

$$d_c = a - x_1 = b - y_1 \ , \qquad (\text{A3})$$

is displayed in Fig. 9. To fix ideas we let $b \geq a$.

By symmetry,

$$\mathbf{H}(x,y,z)=\hat{z}H_z(x,y) \ . \tag{A4}$$

Using Ampère's and Biot-Savart's law, several workers have shown that in the circumstances under consideration the magnetic-field configurations $H_z(x,y)$ are uniform along the current contours defined above.[67–70] Consequently the H profiles can be viewed and expressed in terms of one variable.[70–73] We refer the reader to Fig. 10 for sketches of the profiles and displays of the symbols.

In the outer volume $x_i \leq x \leq a$, filled with flux-retaining critical persistent currents after the removal of H_{cool} or H_{cycle}, Maxwell's equation $\nabla \times \mathbf{H} = \mathbf{j}$ and the critical-state assumption that $j = j_c = \alpha / H^n$ lead to

$$\frac{dH}{dx} = -\frac{\alpha}{H^n} \ . \tag{A5}$$

Integration yields

$$H_2^{n+1}(x) = H_{*g}^{n+1}\left[1-\frac{x}{a}\right] , \tag{A6}$$

where

$$H_{*g}^{n+1} = (n+1)\alpha a \ . \tag{A7}$$

Although we retain the subscript g for grains, the model developed here applies also to homogeneous bulk specimens.

In the H_{cool} procedure,

$$H_1(x) = H_{\text{cool}} \tag{A8}$$

in the inert inner volume $0 \leq x \leq x_i$. Since $H_2(x_i) = H_{\text{cool}}$ when $0 < H_{\text{cool}} \leq H_{*g}$, then

$$\frac{x_i}{a} = 1 - \left[\frac{H_{\text{cool}}}{H_{*g}}\right]^{n+1} . \tag{A9}$$

The inert region vanishes when $H_{\text{cool}} \geq H_{*g}$.

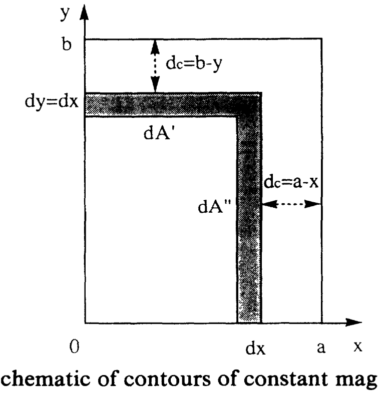

FIG. 9. Schematic of contours of constant magnetic flux density at a distance d_c from the surface of an isotropic rectangular grain of thickness $2a$ along the x axis, width $2b$ along y (with $b \geq a$), and infinite length parallel to a homogeneous applied field along the z axis. From conservation of current, $j_{cx}\Delta y \Delta z = j_{cy}\Delta x \Delta z$ with $j_{cx} = j_{cy}$ for isotropic grain.

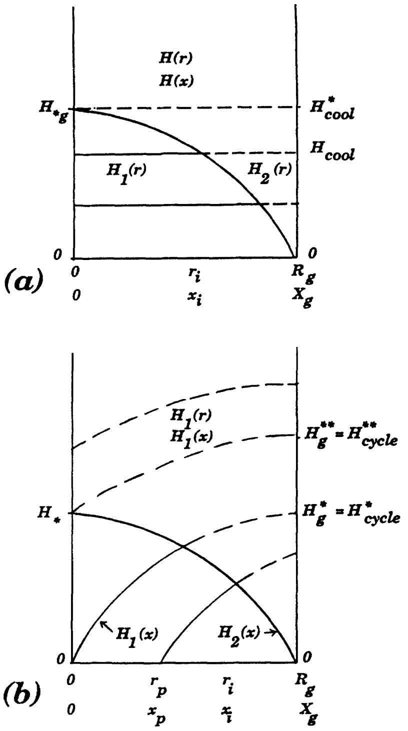

FIG. 10. Schematic of $H(r)$ profiles between the center and the surface $x = a = X_g = R_g$ of the isotropic grain depicted in Fig. 9. (a) Profiles after field cooling and after removal of H_{cool} (horizontal dashed curves and solid curves, respectively). (b) Profiles when H_{cycle} is present (dashed curves) and after removal of H_{cycle} (solid curves). $x_i(r_i)$ denote the intersection of the initial and final profiles. $x_p(r_p)$ denote the surface of penetration of the profiles.

In the H_{cycle} procedure, the inner region $x_p \leq x \leq x_i$ is filled with shielding critical persistent currents. Here, integration of Eq. (A5) with a change of sign yields

$$H_1^{n+1}(x) = H_{\text{cycle}}^{n+1} - H_{*g}^{n+1}\left[1-\frac{x}{a}\right] . \tag{A10}$$

The requirement that $H_1(x_i) = H_2(x_i)$ at the intersection of two profiles [Eqs. (A6) and (A10)] gives

$$\frac{x_i}{a} = 1 - \frac{1}{2}\left[\frac{H_{\text{cycle}}}{H_{*g}}\right]^{n+1} , \tag{A11}$$

which applies until $x_i = 0$. The field-shielding region vanishes when

$$H_{\text{cycle}} \geq 2^{1/(n+1)} H_{*g} = H^{**}_{\text{cycle}} = H_{**g} \ . \tag{A12}$$

The condition that $H_1(x) = 0$ at $x = x_p$ leads to

$$\frac{x_p}{a} = 1 - \left[\frac{H_{\text{cycle}}}{H_{*g}}\right]^{n+1} , \tag{A13}$$

applicable over the range $0 < H_{\text{cycle}} \leq H_{*g}$. The field-shielding inner region shrinks from a width $a/2$ to 0 as $H_{*g} \leq H_{\text{cycle}} \leq H_{**g}$ is removed, where

$$H_{**g}^{n+1} = 2H_{*g}^{n+1} = 2(n+1)\alpha a \ . \tag{A14}$$

Equation (A14) follows from letting $H_1(x) = H_{*g}$ at $x = 0$

in Eq. (A10).

The element of area dA threaded by a uniform magnetic flux density is depicted in Fig. 9. The infinitesimal width of dA', the horizontal segment of dA in the sketch, is written dx since the $H(x,y)$ profiles depend on the variable x. Consequently, we write

$$dA = dA' + dA'' = \{(b-a)+2x\}dx\ , \tag{A15}$$

where

$$dA' = x\,dx\ , \tag{A16}$$

$$dA'' = y\,dx = (b-d_c)dx = \{b-(a-x)\}dx\ . \tag{A17}$$

The spatial average of the trapped magnetic field is obtained from the definition

$$\begin{aligned}\langle H\rangle ab &= \int_0^a\int_0^b H(x,y)dA\\ &= \int_0^{x_i} H_1(x)\{(b-a)+2x)\}dx\\ &\quad+\int_{x_i}^a H_2(x)\{(b-a)+2x)\}dx\ .\end{aligned} \tag{A18}$$

Introducing the expressions for $H_1(x)$, $H_2(x)$, x_p, and x_i developed above and integrating leads to the following formulas for $M_g=\langle H\rangle$ for the cases where $n=0$ and 1 for the $H_{\rm cool}$ and $H_{\rm cycle}$ procedures. For brevity we write

$$u=\frac{H_{\rm cool}}{H_{*g}}=\frac{H_{\rm cycle}}{H_{*g}}\ . \tag{A19}$$

$H_{\rm cool}$ procedure

For the Bean approximation ($n=0$),

$$\frac{M_{\rm gr}}{H_{*g}}=u-\frac{1}{2}\left[1+\frac{a}{b}\right]u^2+\frac{1}{3}\left[\frac{a}{b}\right]u^3\ , \tag{A20}$$

which simplifies to

$$\frac{M_{\rm gr}}{H_{*g}}=u-\tfrac{1}{2}u^2 \tag{A21}$$

for an infinite slab where $b\rightarrow\infty$, and to

$$\frac{M_{\rm gr}}{H_{*g}}=u-u^2+\tfrac{1}{3}u^3 \tag{A22}$$

for a square and a cylinder. For the Kim approximation ($n=1$),

$$\frac{M_{\rm gr}}{H_{*g}}=u-\frac{1}{3}\left[1+\frac{a}{b}\right]u^3+\frac{1}{5}\left[\frac{a}{b}\right]u^5\ , \tag{A23}$$

which reduces to

$$\frac{M_{\rm gr}}{H_{*g}}=u-\tfrac{1}{3}u^3 \tag{A24}$$

for an infinite slab, and

$$\frac{M_{\rm gr}}{H_{*g}}=u-\tfrac{2}{3}u^3+\tfrac{1}{5}u^5 \tag{A25}$$

for a square and a cylinder.

Equations (A20)–(A25) apply over the range $0\le u\le 1$.

$H_{\rm cycle}$ procedure

As indicated earlier in this Appendix, two ranges of the variable $u=H_{\rm cycle}/H_{*g}$ need to be considered in this procedure. For the Bean approximation,

$$\frac{M_{\rm gr}}{H_{*g}}=\frac{1}{4}\left\{u^2+\frac{a}{b}(u^2-u^3)\right\}\ , \tag{A26}$$

applicable over the range $0\le u\le 1$, and

$$\frac{M_{\rm gr}}{H_{*g}}=-\frac{1}{2}+u-\frac{u^2}{4}+\frac{a}{b}\left[\frac{1}{6}-\frac{u^2}{4}+\frac{u^3}{12}\right]\ , \tag{A27}$$

applicable over the range $1\le u\le 2$. The reader can readily verify that the two expressions correspond when $u=1$ and extract the formulas for the infinite slab and the square (and hence the cylinder) by letting $b\rightarrow\infty$ and $a=b$.

For the Kim approximation,

$$\frac{M_{\rm gr}}{H_{*g}}=\frac{\sqrt{2}}{3}\left\{u^3+\frac{a}{b}(u^3-u^5)\right\}\ , \tag{A28}$$

applicable over the range $0\le u\le 1$, and

$$\begin{aligned}\frac{M_{\rm gr}}{H_{*g}}=\frac{\sqrt{2}}{3}\Bigg\{&u^3-\sqrt{2}(u^2-1)^{3/2}+\frac{a}{b}(u^3-u^5)\\ &+\frac{\sqrt{2}}{5}\left[\frac{a}{b}\right](1+4u^4)(u^2-1)^{3/2}\Bigg\}\ ,\end{aligned} \tag{A29}$$

applicable over the range $1\le u\le\sqrt{2}$. Again the reader can readily verify that Eqs. (A28) and (A29) correspond when $u=1$ and extract the formulas for the infinite slab and square (cylinder) from these expressions.

Equations (A20)–(A29) are displayed in Fig. 11 for the limiting geometries [infinite slab and cylinder (square)]. In the displays $M_{\rm gr}$ is normalized to the corresponding saturation (i.e., plateau) value since that is the appropriate reference "level" in the analysis and comparison of measurements. We note that the "structure" of the curves is not very sensitive to the choice of geometry or of dependence of j_c on B.

For the calculations of $\langle B_z\rangle_{\rm hole}$ and $\langle B_z\rangle_{\rm wall}$ displayed in Figs. 1–4, we exploit the expressions for infinite slab geometry and the Bean approximation. We assume, for simplicity, that all the grains in the wall of the tube are initially immersed in the externally applied $H_{\rm cool}$ and $H_{\rm cycle}$. We note that Eqs. (20)–(29), (34), and (37) only apply after removal of $H_{\rm cool}\ge H_{*m}$ and $H_{\rm cycle}\ge 2^{1/(n+1)}H_{*m}$. Consequently, in the calculations of $H_{\rm gr}$, the baseline is displaced and here,

$$u=\frac{(H_{\rm cool}-H_{*m})}{H_{*g}}\ \text{or}\ u=\frac{(H_{\rm cycle}-2^{1/(n+1)}H_{*m})}{H_{*g}}\ . \tag{A30}$$

Such a displacement of the baseline does not affect the above formulas nor alter the results in the Bean approximation, since here j_{cg} is independent of B. When the function under scrutiny is $M_{\rm gr}$ [see Eqs. (34) and (42)],

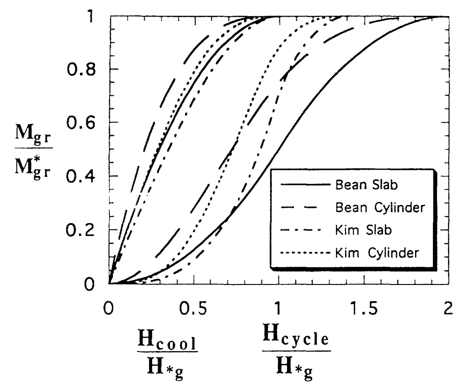

FIG. 11. Evolution of $M_{\rm gr}$, the remanent magnetization in an infinite slab and cylinder, after removal of $H_{\rm cool}$ and $H_{\rm cycle}$. The curves were calculated using the expressions developed in this Appendix using $n=0$ (Bean) and $n=1$ (simple Kim approximation) for $j_{cg}=\alpha/H^n$. $M_{\rm gr}$ is normalized to $M^*_{\rm gr}$, the corresponding maximum remanent magnetization for each geometry and choice of n. $H_{\rm cool}$ and $H_{\rm cycle}$ are normalized to H_{*g}, the first full penetration field for the corresponding choice of n. Note that the "double" penetration field $H^{**}_{\rm cycle}=2H^*_{\rm cycle}=2H_{*g}$ when $n=0$ and $H^{**}_{\rm cycle}=\sqrt{2}H^*_{\rm cycle}=\sqrt{2}H_{*g}$ when $n=1$. The display we use corresponds to the situation confronting the experimental worker in comparing $H_{\rm cool}$ and $H_{\rm cycle}$ data on a given specimen of known geometry but unknown dependence of j_{cg} on B. The ratios of $H_{\rm cycle}$ and $H_{\rm cool}$ for the onset of the two plateaus provide a simple and direct guide to the dependence of j_{cg} on B.

these "floors" do not apply and the baseline is not "shifted."

APPENDIX B

For completeness, in this Appendix, we develop expressions for the remanent $H_m(r)$ profiles and $\langle B_z\rangle_{\rm hole}/\mu_0=H_m(R_i)$ for infinite tubes, where

$$j_c(r)=j_{c0}e^{-H_{\rm total}(r)/H_0} . \tag{B1}$$

Here j_{c0} and H_0 are temperature-dependent parameters of the matrix.

$$H_{\rm total}(r)=\begin{cases} H_{\rm gr}-H_m(r) & \text{when } H_{\rm gr}>H_m(r) , & \text{(B2a)}\\ H_m(r)-H_{\rm gr} & \text{when } H_{\rm gr}<H_m(r) . & \text{(B2b)}\end{cases}$$

All quantities are absolute values and $H_{\rm gr}$ is assumed uniform. Maxwell's equation, Eqs. (B1) and (B2a), and the critical-state assumption lead to

$$\int_r^{R_o} e^{[H_{\rm gr}-H_m(r)]/H_0} d\{[H_{\rm gr}-H_m(r)]/H_0\} =(j_{c0}/H_0)\int_r^{R_o} dr , \tag{B3}$$

which yields

$$H_m(r)=H_{\rm gr}-H_0\ln\{e^{H_{\rm gr}/H_0}-[j_{c0}(R_o-r)/H_0]\} , \tag{B4}$$

since $H_m(R_o)=0$ after removal of $H_{\rm cool}$ or $H_{\rm cycle}$. Equation (B4) applies to the outer zone $r_o\le r\le R_o$, where $H_{\rm gr}\ge H_m(r)$ and to the entire wall when $H_{\rm gr}\ge H_m(R_i)$ hence $r_o=R_i$.

For the inner zone $R_i\le r\le r_o$ where $H_m(r)\ge H_{\rm gr}$, Eq. (B2b) applies. This leads to

$$\int_{R_i}^{r} e^{[H_m(r)-H_{\rm gr}]/H_0} d\{[H_m(r)-H_{\rm gr}]/H_0\} =-(j_{c0}/H_0)\int_{R_i}^{r} dr , \tag{B5}$$

which yields

$$H_m(r)=H_{\rm gr}+H_0\ln\{e^{[H_m(R_i)-H_{\rm gr}]/H_0} -[j_{c0}(r-R_i)/H_0]\} . \tag{B6}$$

Since $H_{\rm total}=0$ at $r=r_o$, the interface between the two zones and hence $H_m(r_o)=H_{\rm gr}$, Eqs. (B4) and (B6) give

$$(j_{c0}r_o/H_0)=1+(j_{c0}R_o/H_0)-e^{H_{\rm gr}/H_0} =e^{[H_m(R_i)-H_{\rm gr}]/H_0}-1+(j_{c0}R_i/H_0) . \tag{B7}$$

Solving for $H_m(R_i)$ yields

$$H_m(R_i)=H_{\rm gr}+H_0\ln\{2+[j_{c0}(R_o-R_i)/H_0] -e^{H_{\rm gr}/H_0}\} . \tag{B8}$$

Introducing (B8) into (B7) gives

$$H_m(r)=H_{\rm gr}+H_0\ln\{2+[j_{c0}(R_o-r)/H_0]-e^{H_{\rm gr}/H_0}\} . \tag{B9}$$

Letting $dH_m(R_i)/dH_{\rm gr}=0$, we find that $H_m(R_i)$ traverses a maximum when

$$\frac{H_{\rm gr}}{H_0}=\ln\{1+\tfrac{1}{2}[j_{c0}(R_o-R_i)/H_0]\} . \tag{B10}$$

Hence,

$$I^*_{c,\max}\equiv H_m(R_i)_{\max} =2H_0\ln\{1+\tfrac{1}{2}[j_{c0}(R_o-R_i)/H_0]\} . \tag{B11}$$

From Eq. (B8) when $H_{\rm gr}=0$ and hence $M_{\rm gr}=0$, we see that, here,

$$H_m(R_i)=H_{*m} \equiv I^*_c(0) =H_0(\ln 2+\ln\{1+\tfrac{1}{2}[j_{c0}(R_o-R_i)/H_0]\}) . \tag{B12}$$

Consequently,

$$\frac{I^*_{c,\max}}{I^*_c(0)}=\frac{2}{1+\ln 2/\ln\{1+\frac{1}{2}[j_{c0}(R_o-R_i)/H_0]\}} , \tag{B13}$$

which rises to a maximum value of 2 as $j_{c0}(R_o-R_i)/H_0$ becomes infinite.

APPENDIX C

Among the B profiles sketched in Fig. 6, that labeled (2) "embraces" the maximum total magnetic flux. Consequently, $\mu_0\langle H_m(r)\rangle$, the remanent magnetic flux density permeating the matrix, traces a peak as a function of $H_{\rm gr}$, i.e., vs $M_{\rm gr}$ and therefore vs $H_{\rm cool}$ and $H_{\rm cycle}$ when j_{cm}, the critical current density, decreases as B increases. In this Appendix we develop expressions for $\langle H_m(r)\rangle$ for a thin-walled tube where $j_{cm}=\alpha/H^n_{\rm total}$ in the framework of our simple model where $H_{\rm gr}$ is assumed uniform. For the case where $n=1$ we develop an expression for the maximum value of $\langle H_m(r)\rangle$ and the corresponding $H_{\rm gr}$.

For a thin-walled tube,

$$\langle H_m(r)\rangle=\frac{2}{(R_o^2-R_i^2)}\int_{R_i}^{R_o}H_m(r)r\,dr \approx\frac{1}{X}\int_{R_i}^{R_o}H_m(x)dx\ , \tag{C1}$$

where $R_o-R_i=X\ll R_i$. In the context of planar geometry, Eqs. (20) and (28) read

$$H_m(x)_2=H_{\rm gr}-\left\{H_{\rm gr}^{n+1}-H_{*n}^{n+1}\left[1-\frac{x}{X}\right]\right\}^{1/(n+1)}\ , \tag{C2}$$

$$H_m(x)_1=H_{\rm gr}+\left\{H_{*m}^{n+1}\left[1-\frac{x}{X}\right]-H_{\rm gr}^{n+1}\right\}^{1/(n+1)}\ , \tag{C3}$$

where Eq. (C2) applies to the outer zone $x_{0\le}x\le X$, and Eq. (C3) applies to the inner zone $0\le x\le x_0$, with

$$1-\frac{x_0}{X}=\left[\frac{H_{\rm gr}}{H_{*m}}\right]^{n+1}\ . \tag{C4}$$

Introducing Eqs. (C2)–(C4) into the definition

$$\langle H_m(x)\rangle=\int_0^{x_0}H_m(x)_1d(x/X)+\int_{x_0}^{X}H_m(x)_2d(x/X)\ , \tag{C5}$$

we obtain

$$\frac{\langle H_m(x)\rangle}{H_{*m}}=\left[\frac{n+1}{n+2}\right]\left[\left\{1-\left[\frac{H_{\rm gr}}{H_{*m}}\right]^{n+1}\right\}^{(n+2)/(n+1)} -\left[\frac{H_{\rm gr}}{H_{*m}}\right]^{n+2}\right]+\frac{H_{\rm gr}}{H_{*m}}\ . \tag{C6}$$

$\langle H_m(x)\rangle$ transverses a maximum when $H_{\rm gr}$ satisfies the equation

$$\left[\frac{H_{\rm gr}}{H_{*m}}\right]^{n}\left\{1-\left[\frac{H_{\rm gr}}{H_{*m}}\right]^{n+1}\right\}^{1/(n+1)} +\left[\frac{H_{\rm gr}}{H_{*m}}\right]^{n+1}=\frac{1}{n+1}\ . \tag{C7}$$

For the simple Kim case where $j_{cm}=\alpha/H_{\rm total}$, Eq. (C7) yields

$$H_{\rm gr}=H_{*m}\left\{\frac{1}{2}-\frac{\sqrt{2}}{4}\right\}^{1/2}=0.383H_{*m}\ . \tag{C8}$$

Introducing this into Eq. (C6) gives

$$\frac{\langle H_m(x)\rangle_{\rm max}}{H_{*m}}=0.871 \text{ and } \frac{\langle H_m(x)\rangle_{\rm max}}{\langle H_m(x)\rangle_0}=1.307\ ,$$

where $\langle H_m(x)\rangle_0$ is the spatial average of the magnetic field when $H_{\rm gr}=0$ [curve labeled (1) in Fig. 6].

---

[1] J. O. Willis, M. E. McHenry, M. P. Maley, and H. Sheinberg, IEEE Trans. Magn. **25**, 2502 (1989).

[2] Wang Jingrong, Li Jianping, Yang Wanming, and Zhou Lian, IEEE Trans. Magn. **27**, 1029 (1991).

[3] Yunhui Xu, J. Appl. Phys. **69**, 2740 (1991).

[4] F. J. Eberhardt, A. D. Hibbs, and A. M. Campbell, IEEE Trans. Magn. **25**, 2146 (1989).

[5] M. R. Cimberle, C. Ferdeghini, G. L. Nicchiotti, M. Putti, A. S. Siri, C. Rizzuto, C. A. Costa, M. Ferretti, C. L. Olcese, F. C. Matacotta, and E. Olzi, Supercond. Sci. Technol. **1**, 30 (1988). Inspection of their Fig. 5 reveals that $\langle B_z\rangle_{\rm hole}$, the remanent flux density in the cavity, reverses sign as $\mu_0H_{\rm cycle}$ is augmented from 4 to 9.6 mT.

[6] Yu. A. Bashkirov, L. S. Fleishman, T. Yu. Patsayeva, A. N. Solbelev, and A. B. Vdovin, IEEE Trans. Magn. **27**, 1089 (1991).

[7] C. P. Bean and M. V. Doyle, J. Appl. Phys. **33**, 3334 (1962).

[8] J. R. Cave, W. A. Willen, Y. Brissette, and C. Richer, in *Proceedings of the 13th International Conference on Magnet Technology MT13, Victoria, B.C., Canada, 1993* [IEEE Trans. Magn. (to be published)].

[9] J. R. Clem, M. M. Fang, S. L. Miller, J. S. Ostenson, Z. X. Zhao, and D. K. Finnemore, Appl. Phys. Lett. **47**, 1224 (1985).

[10] J. M. Corsan, G. W. Coles, and H. J. Goldsmid, Br. J. Appl. Phys. **15**, 1383 (1964).

[11] P. Fournier, M. Oussena, and M. Aubin, Cryogenics **33**, 333 (1993).

[12] C. E. Gough, A. Gencer, G. Yang, M. Z. Shoustari, A. I. M. Rae, and J. S. Abell, Cryogenics **33**, 339 (1993).

[13] A. F. Hildebrandt, D. D. Elleman, F. C. Whitmore, and R. Simpkins, J. Appl. Phys. **33**, 2375 (1962).

[14] M. Ishii, K. Tsukamoto, H. Shimojima, C. Yamagishi, M. Takata, and T. Yamashita, Jpn. J. Appl. Phys. **33**, 1310 (1992).

[15] J. Jung, I. Isaac, and M. A. K. Mohamed, Cryogenics **32**, 988 (1992).

[16] A. R. Kuper, H. Hemmes, and H. Rogalla, Cryogenics **32**, 1027 (1992).

[17] Y. B. Kim, C. F. Hempstead, and A. R. Strnad, Phys. Rev. **131**, 2486 (1963).

[18] A. S. Kheifets, A. I. Veinger, and L. G. Paritsky, Physica C **174**, 86 (1991).

[19] M. A. K. Mohamed and J. Jung, Phys. Rev. B **44**, 4512 (1991).

[20] V. Plechacek, Cryogenics **32**, 1010 (1992).

[21] Mario Rabinowitz, H. W. Arrowsmith, and S. D. Dahlgren, Appl. Phys. Lett. **30**, 607 (1977).

[22] T. Sasaki, M. Tanaka, M. Morita, K. Miyamoto, and M. Hashimoto, Jpn. J. Appl. Phys. **31**, 1026 (1992).

[23] S. Senoussi, S. Hadjoudj, C. Weyl, and J. P. Fondere, Physica C **165**, 199 (1990).

[24] P. S. Swartz and C. H. Rosner, J. Appl. Phys. **32**, 2292 (1962).

[25] O. G. Symko, W. J. Yeh, D. J. Zheng, and S. Kulkarni, J. Appl. Phys. **65**, 2142 (1989).

[26] E. Tjukanov, R. W. Cline, R. Krahn, M. Hayden, M. W. Rey-

nolds, W. N. Hardy, J. F. Carolan, and R. C. Thompson, Phys. Rev. B **36**, 7244 (1987).

[27] K. Tsukamoto, M. Ishii, H. Shimojima, C. Yamagishi, M. Takata, and T. Yamashita, Jpn. J. Appl. Phys. **31**, L464 (1992).

[28] E. S. Vlakhov, V. T. Kovachev, M. Polak, M. Majoros, Y. B. Dimitriev, S. Jambazov, E. Kashchieva, and A. Staneva, Physica C **175**, 335 (1991).

[29] J. R. Clem, Physica C **153**, 50 (1988).

[30] H. Dersch and G. Blatter, Phys. Rev. B **38**, 11 391 (1988).

[31] K. E. Hautanen, M. Oussena, and J. R. Cave, Cryogenics **33**, 326 (1993).

[32] L. Ji, M. S. Rzchowski, N. Anand, and M. Tinkham, Phys. Rev. B **47**, 470 (1993).

[33] K. I. Kugel and A. L. Rakhmanov, Physica C **196**, 17 (1992).

[34] K.-H. Muller, J. C. MacFarlane, and R. Driver, Physica C **158**, 69 (1989).

[35] In-Gann Chen, Jianxiong Liu, Roy Weinstein, and Kwong Lau, J. Appl. Phys. **72**, 1013 (1992).

[36] M. Daümling, E. Sarnelli, P. Choudhari, A. Gupta, and J. Lacey, Appl. Phys. Lett. **61**, 1355 (1992).

[37] L. M. Fisher, V. S. Gorbachev, N. V. Il'in, N. M. Makarov, I. F. Voloshin, V. A. Yampol'skii, R. L. Snyder, S. T. Misture, M. A. Rodriguez, D. P. Matheis, V. R. W. Amarakoon, J. G. Fagan, J. A. Taylor, and A. M. M. Barus, Phys. Rev. B **46**, 10 986 (1992).

[38] E. Altshuler, J. Musa, J. Barroso, A. R. R. Papa, and V. Venegas, Cryogenics **33**, 308 (1993).

[39] Uri Dai, Guy Deutscher, Claude Lacour, Francine Laher-Lacour, Philippe Mocaer, and Michel Lagues, Appl. Phys. Lett. **56**, 284 (1990).

[40] J. E. Evetts and B. A. Glowacki, Cryogenics **28**, 641 (1988).

[41] B. A. Glowacki, J. Jackiewicz, and J. E. Evetts, Cryogenics **33**, 86 (1993).

[42] A. R. Jones, R. A. Doyle, F. J. Blunt, and A. M. Campell, Physica C **196**, 63 (1992).

[43] K. Kwasnitza and Ch. Widmer, Cryogenics **29**, 1035 (1989); IEEE Trans. Magn. **27**, 1202 (1991).

[44] M. Majoros, M. Polak, V. Strbik, S. Benacka, S. Chromik, F. Hanic, and V. Plechacek, Supercond. Sci. Technol. **3**, 227 (1990).

[45] M. E. McHenry, M. P. Maley, and J. O. Willis, Phys. Rev. B **40**, 2666 (1989).

[46] Philippe Mocaer, Leondro Tessler, Michel Lagues, Francine Laher-Lacour, Claude Lacour, Uri Dai, N. Hess, and Guy Deutscher, Physica C **185-189**, 2505 (1991).

[47] K.-H. Muller and D. N. Matthews, Physica C **206**, 275 (1993).

[48] Y. Nakagawa, H. Yamasaki, M. Umeda, and S. Kosaka, J. Appl. Phys. **71**, 800 (1992).

[49] B. Ullmann and H. C. Freyhardt, Cryogenics **32**, 1109 (1992).

[50] K. Watanabe, K. Noto, H. Morita, F. Fujimori, K. Mizuno, T. Aomine, B. Ni, T. Matsushita, K. Yamafuji, and Y. Muto, Cryogenics **29**, 263 (1989).

[51] K. Mendelssohn, Proc. R. Soc. London Ser. A **152**, 34 (1935); Cryogenics **3**, 129 (1963).

[52] K. Mendelssohn and J. R. Moore, Nature **135**, 826 (1935).

[53] E. H. Brandt, Phys. Rev. Lett. **71**, 2821 (1993).

[54] E. H. Brandt and M. Indenbom, Phys. Rev. B **48**, 12 893 (1993).

[55] L. W. Conner and A. R. Malozemoff, Phys. Rev. B **43**, 402 (1991).

[56] M. Daümling and D. C. Larbalestier, Phys. Rev. B **40**, 9350 (1989).

[57] H. Hemmes, A. R. Kuper, and L. J. M. van de Klundert, IEEE Trans. Magn. **27**, 1069 (1991).

[58] M. L. Hodgdon, R. Navarro, and L. J. Campbell, Europhys. Lett. **16**, 677 (1991).

[59] R. Navarro and L. J. Campbell, Phys. Rev. B **44**, 10 146 (1991).

[60] H. Theuss, A. Forkl, and H. Kronmüller, Physica C **190**, 345 (1992).

[61] G. Waysand, Europhys. Lett. **5**, 73 (1988).

[62] A. Weyers, H. Kliem, J. Lützner, and G. Artl, J. Appl. Phys. **71**, 5089 (1992).

[63] J. Zhu, J. Mester, J. Lockhart, and J. Turneaure, Physica C **212**, 216 (1993).

[64] U. Yaron, Y. Kornyushin, and I. Felner, Phys. Rev. B **46**, 14 823 (1992).

[65] Ming Xu, Phys. Rev. B **44**, 2713 (1991). Figure 2 of this paper is incorrect. For correct schematics see our Fig. 10(b).

[66] Ming Xu, A. Umezawa, and G. W. Crabtree, Phys. Rev. B **46**, 11 928 (1992). Figure 3 of this paper is incorrect. For correct schematics, see our Fig. 10(b).

[67] K. Fillmore, Am. J. Phys. **53**, 782 (1985).

[68] W. Hauser, Am. J. Phys. **53**, 774 (1985).

[69] F. Munley, Am. J. Phys. **53**, 779 (1985).

[70] K. V. Bhagwat and P. Chaddah, Phys. Rev. B **44**, 6950 (1991); Physica C **166**, 1 (1990).

[71] D.-X. Chen and R. B. Goldfarb, J. Appl. Phys. **66**, 2489 (1989).

[72] E. M. Gyorgy, R. B. van Dover, K. A. Jackson, L. F. Schneemeyer, and J. V. Waszczak, Appl. Phys. Lett. **55**, 283 (1989).

[73] R. L. Peterson, J. Appl. Phys. **67**, 6930 (1990).

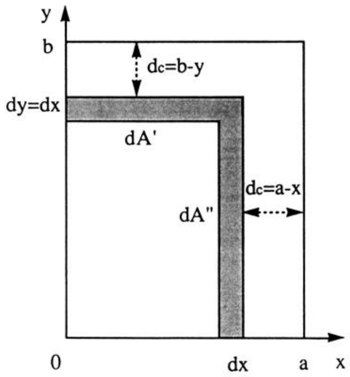

FIG. 9. Schematic of contours of constant magnetic flux density at a distance d_c from the surface of an isotropic rectangular grain of thickness $2a$ along the x axis, width $2b$ along y (with $b \geq a$), and infinite length parallel to a homogeneous applied field along the z axis. From conservation of current, $j_{cx} \Delta y \Delta z = j_{cy} \Delta x \Delta z$ with $j_{cx} = j_{cy}$ for isotropic grain.